Chapter IV

Results and Discussion

4.1 Raw Materials Characterizations.

4.1.1 Chemical Analysis.

Chemical analysis of raw materials from the product data sheet and laboratory testing were shown in Table 9a and 9b respectively.

Table 9. a) Chemical analysis and specifications of three kinds of commercial grade calcined alumina powders ;

% chemical composition	A-11	A-12	A-21
H_2O	–	–	0.040
L.O.I.	0.100	0.010	0.060
Fe_2O_3	0.010	0.010	0.010
SiO_2	0.012	0.020	0.010
Na_2O	0.350	0.300	0.270
Al_2O_3	99.600	99.700	99.700
Physical properties			
Ave. grain dia.[μm.]	50	60	40
Specific gravity [gm./cm.^{3}]	3.92	3.96	3.95
Ultimate α-crystal[μm.]	4-5	5	2-4
Packed bulk density [gm./cm.^{3}]	1.0-1.2	1.0	1.05
Loose bulk density [gm./cm.^{3}]	0.6-0.8	0.7	0.75

Table 9. b) Chemical analysis of other raw materials.

% Element	Bentonite	Ball clay	Wallastonite	Talcum
SiO_2	49.00	51.00	46.90	50.00
Al_2O_3	18.20	30.40	0.17	0.12
Fe_2O_3	0.19	1.90	0.07	0.31
TiO_2	0.02	0.04	0.02	0.02
CaO	5.77	0.40	46.60	0.36
MgO	3.73	0.30	1.84	34.30
Na_2O	0.34	1.40	0.22	0.35
K_2O	0.04	1.30	0.05	0.02
P_2O_5	0.01	_	0.04	0.02
MnO	0.03	_	0.01	0.01
Cr_2O_3	0.01	_	0.01	0.01
L.O.I.	21.20	12.80	3.83	14.00
Sum	98.50	99.54	99.70	99.60

4.1.2 Particle size distribution of alumina powder.

From SEM. micrographs , they were clearly shown that the alumina powders refered to aggromeration of the primary particles. The particle size distribution, measured by sedimentation technique, were presented in the curves in Fig.6

Fig.6 Particle size distribution of alumina powder.

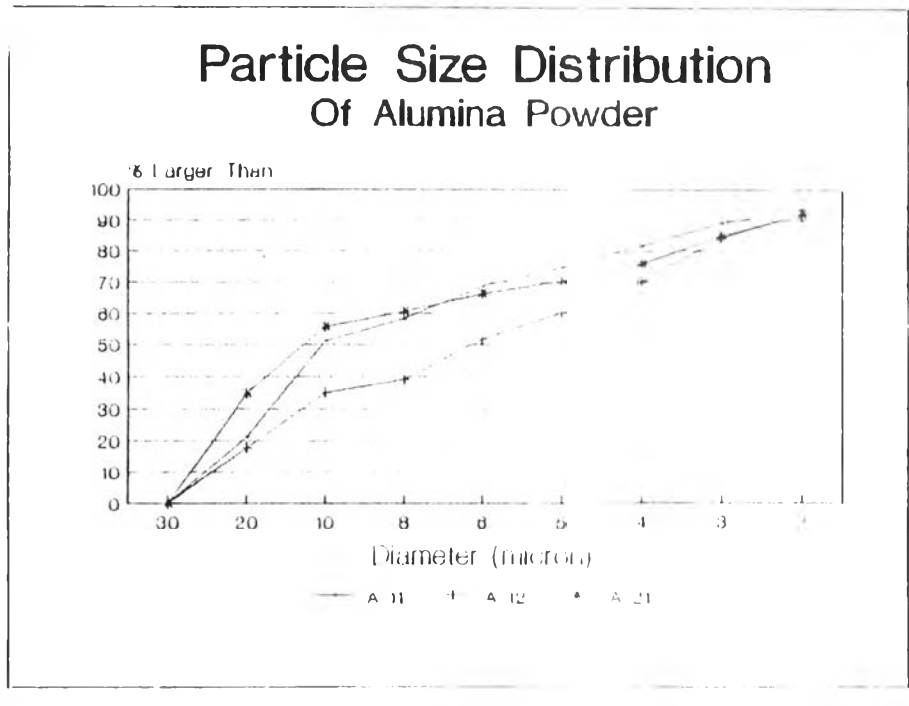

Table 10. Particle size distribution of calcined alumina.

material	20 % by weight finer than [μ m.]
A-11	4.2
A-12	3.5
A-21	3.8

4.1.3 Microstructure of raw materials.

Fig. 7 ; Scanning electron micrographs of calcined alumina powders in the as-recieved condition, showed aggregates of grains which consisted of less than 5 μm. primary particles.

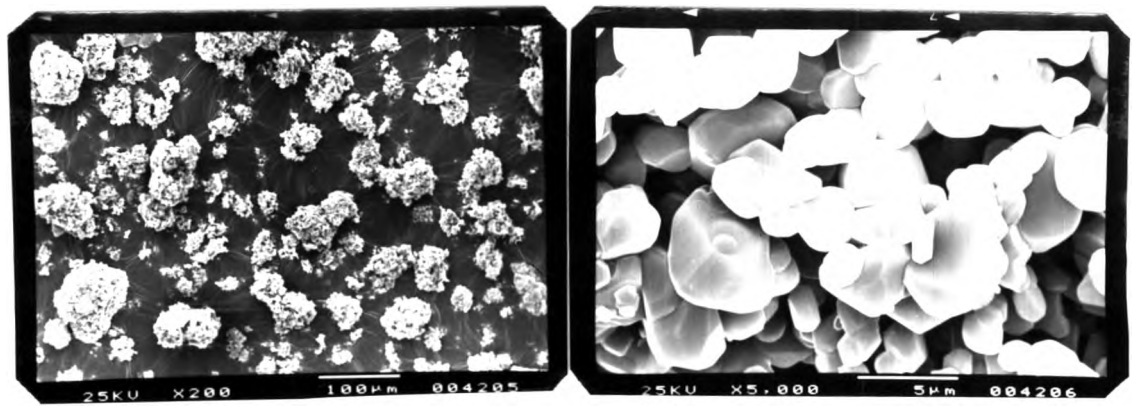

Fig. 7a). Al_2O_3 A-11, Nippon Light Metal Co; Ltd.

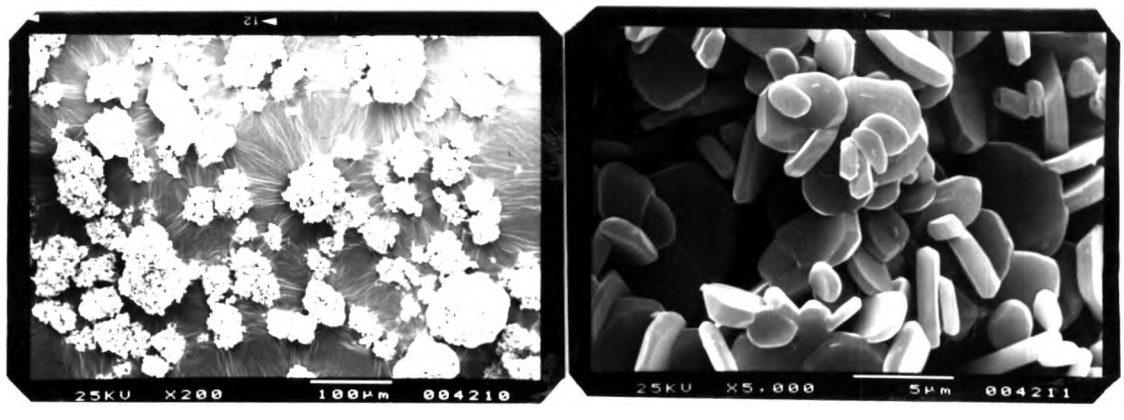

b). Al_2O_3 A-12, Showa Denko Co; Ltd.

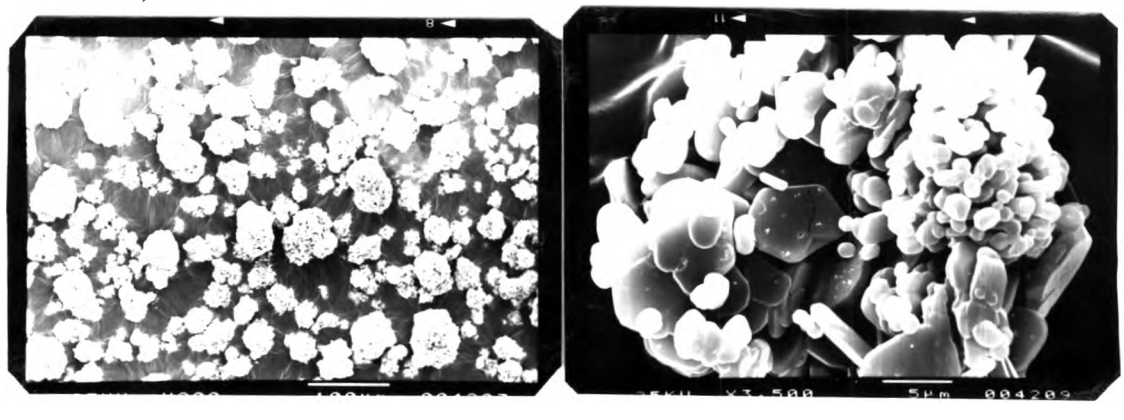

c). Al_2O_3 A-21, Sumitomo Co; Ltd.

—— 100 μm. —— 5 μm.

Scanning electron micrographs of bentonite showed aggregated form, irregular shape particles of the size less than 100 μm.

Fig. 8 SEM micrograph of bentonite.

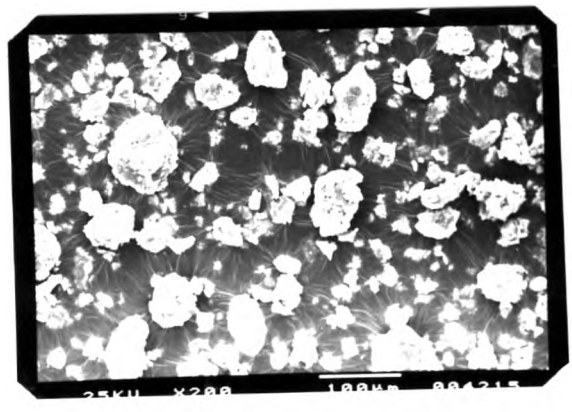

100 μm. ——→

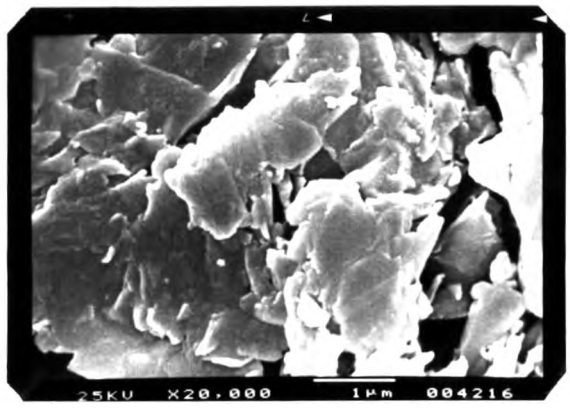

1 μm. ——→

Scanning electron micrograph of ball clay showed irregular shaped particle of hexagonal flake, aggregated form.

Fig. 9 SEM micrograph of ball clay.

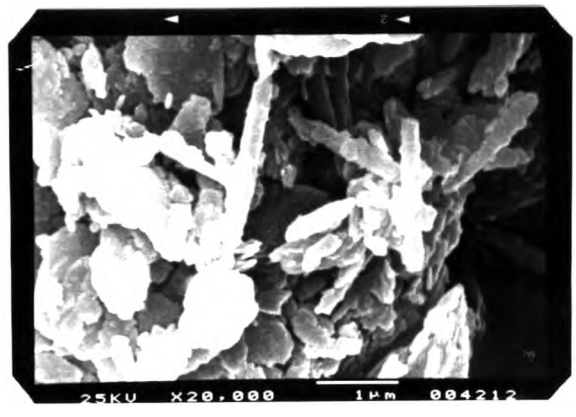

1 µm.

Scanning electron micrograph of talcum showed stacks of unit layers, occured in the form of flake of irregular shape.

Fig.10 SEM micrograph of talcum.

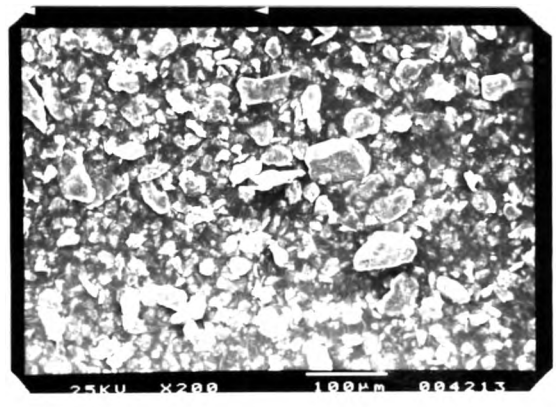

100 µm.

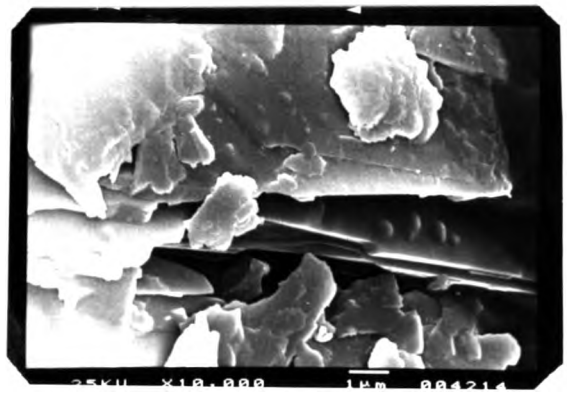

1 µm.

Scanning electron micrograph of wallastonite powder, the particles were fibrous form of long-rod shape, with about 100 μm. in length and 10 m. in width.

Fig.11 SEM micrographs of wallastonite.

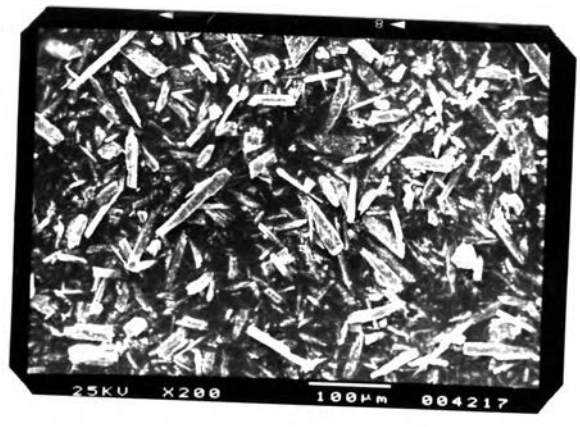

100 μm.

10 μm.

4.1.4 Phase.

From XRD. pattern of calcined alumina powder (A-11) in Fig.12 , the major phase was α-Al_2O_3 which 2θ angles were ;

2θ angle	corresponds to	d-spacing
25.60		3.477
35.20		2.547
37.80		2.378
41.68		2.165
43.40		2.088
46.22		1.964
52.60		1.738
57.50		1.601
59.70		1.545
61.30		1.510

Fig.12 XRD pattern of calcined alumina

✓ = α - Al_2O_3

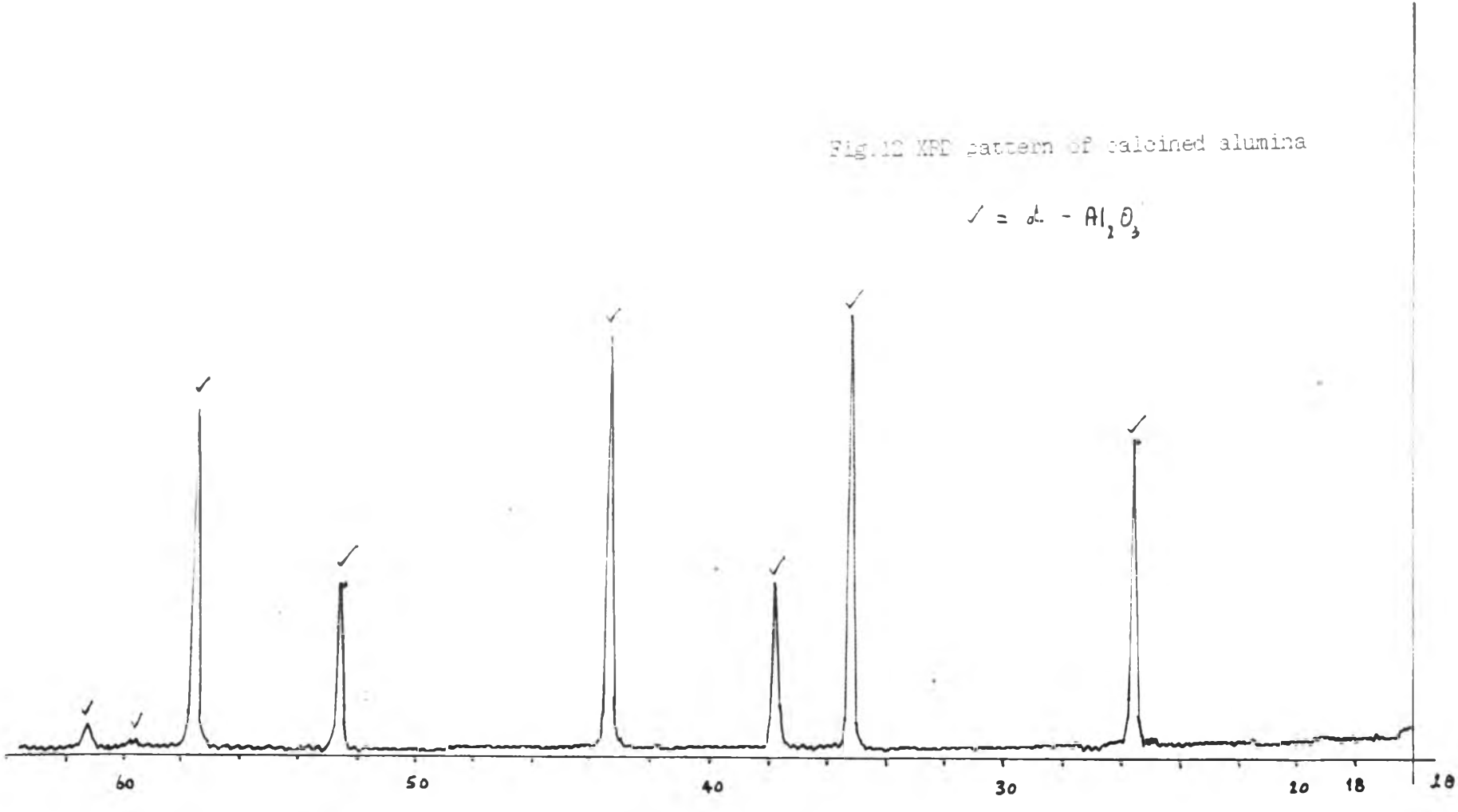

From XRD. pattern of ball clay (MC.) in Fig13. this raw material comprised dominantly kaolinite, subordinate amounts of illites [fine-grain mica] and quartz, and minor to trace amounts of gibbsite and feldspar.

The 2θ angles of kaolinite were ;

2θ angle	correspond to	d-spacing
12.40,		7.132
19.90		4.458
24.90		3.572
35.50		2.527
36.00		2.493
38.50		2.336

The 2θ angles of illite [mica] were ;

2θ angle	correspond to	d-spacing
8.90		9.927
17.80		4.979
19.90		4.458
29.90		2.986
31.30		2.855
32.10		2.786
35.50		2.527

The 2θ angles of quartz were ;

2θ angle	correspond to	d-spacing
20.85		4.257
26.65		3.342
36.70		2.447
39.50		2.279
40.40		2.231
42.60		2.120
45.50		1.992
50.20		1.817
55.00		1.668
60.00		1.541

The 2θ angles of gibbsite were ;

2θ angle	correspond to	d-spacing
18.30		4.844
20.30		4.371
36.70		2.447
37.67		2.386
44.30		2.043

Fig.13 XRD pattern of ball clay [MC]

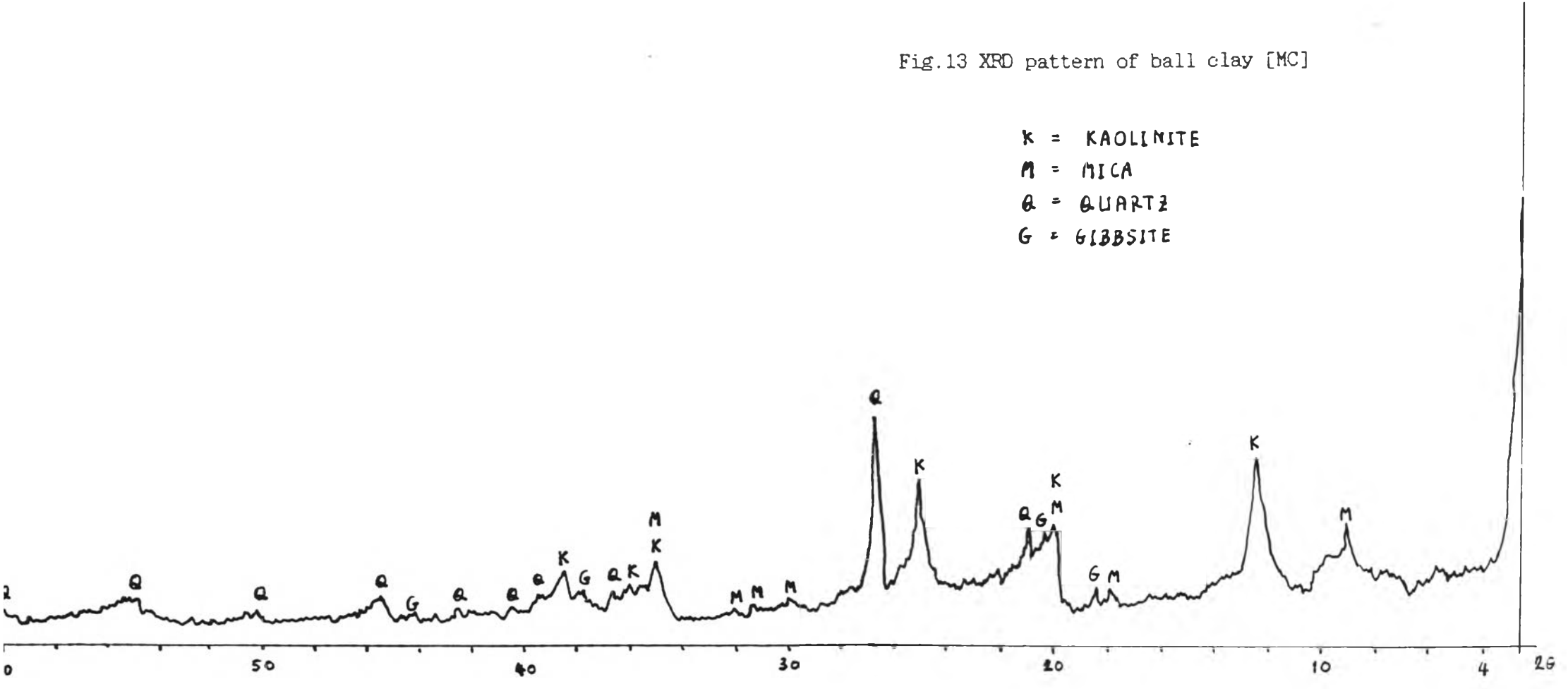

For bentonite, this raw material had two colors happened together, soft-white and soft-pink materials, the XRD. analysis were made seperately.

The XRD. patterns of soft-white material showed that it was composed predominantly of Ca-smectite with minor fluorite and quartz. [Fig.14a)]

The 2θ angles of Ca-smectite in this material were ;

2θ angle	correspond to	d-spacing
5.80		15.224
15.50		5.712
19.80		4.480
29.20		3.056
34.80		2.576
54.20		1.691
62.50		1.485

The 2θ angles of quartz were ;

2θ angle	correspond to	d-spacing
21.00		4.227
27.00		3.299
39.50		2.279
40.50		2.225
42.50		2.125
50.00		1.823
60.00		1.541

The 2θ angles of fluorite were ;

2θ angle	correspond to	d-spacing
28.80		3.097
47.00		1.932
56.00		1.641

For soft-pink material,in Fig.14b),it was composed predomnantly of Ca-smectite with trace fluorite.

The 2θ angles of Ca-smectite were ;

2θ angle	correspond to	d-spacing
6.20		14.243
15.50		5.712
18.00		4.924
27.40		3.252
33.00		2.712
52.20		1.751
60.20		1.536

The 2θ angle of fluorite was 26.40,
corresponded to d-spacing = 3.373

Fig. 14 b) XRD pattern of soft and pink bentonite

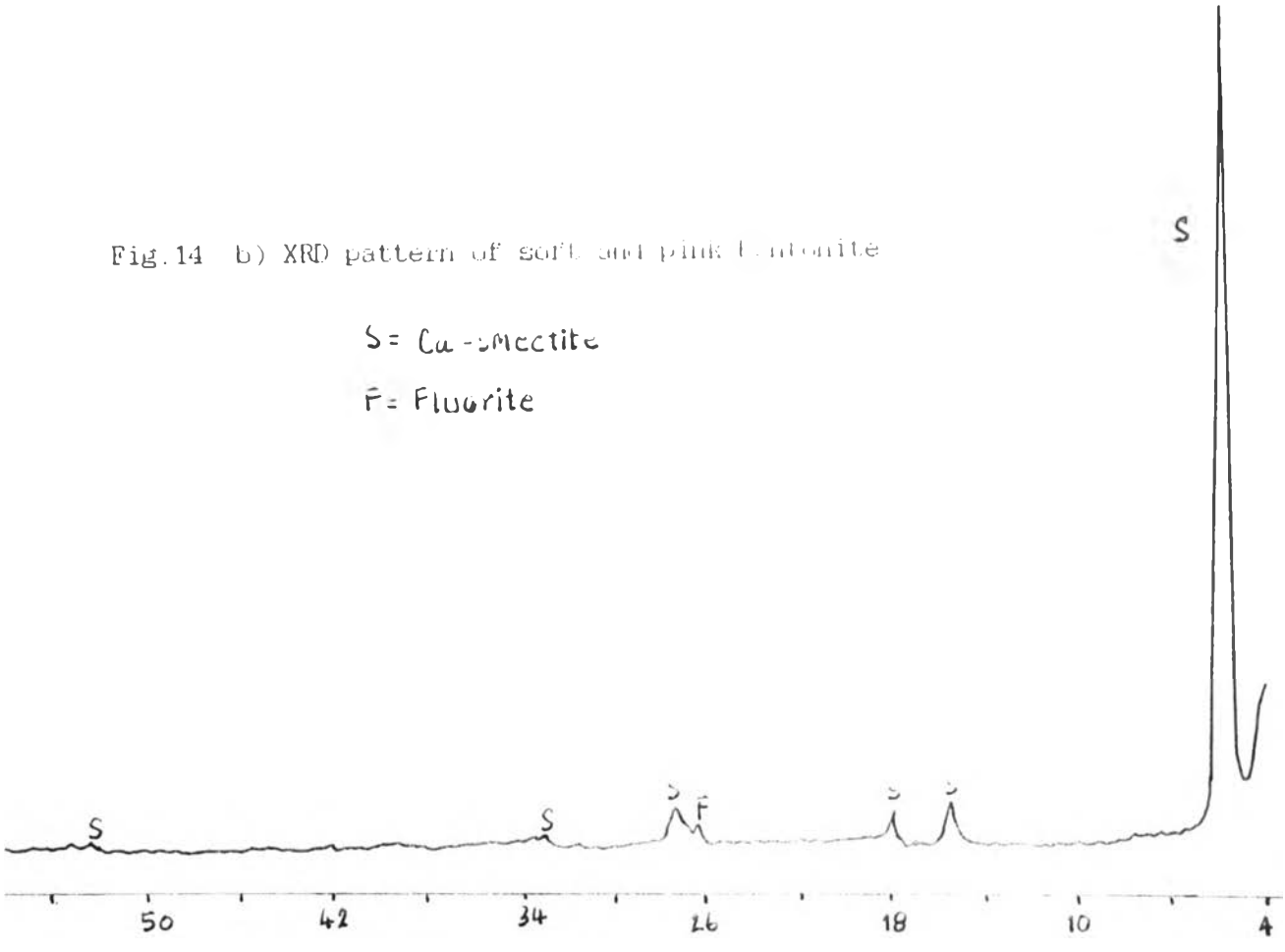

Fig. 14 a) XRD pattern of soft and white bentonite

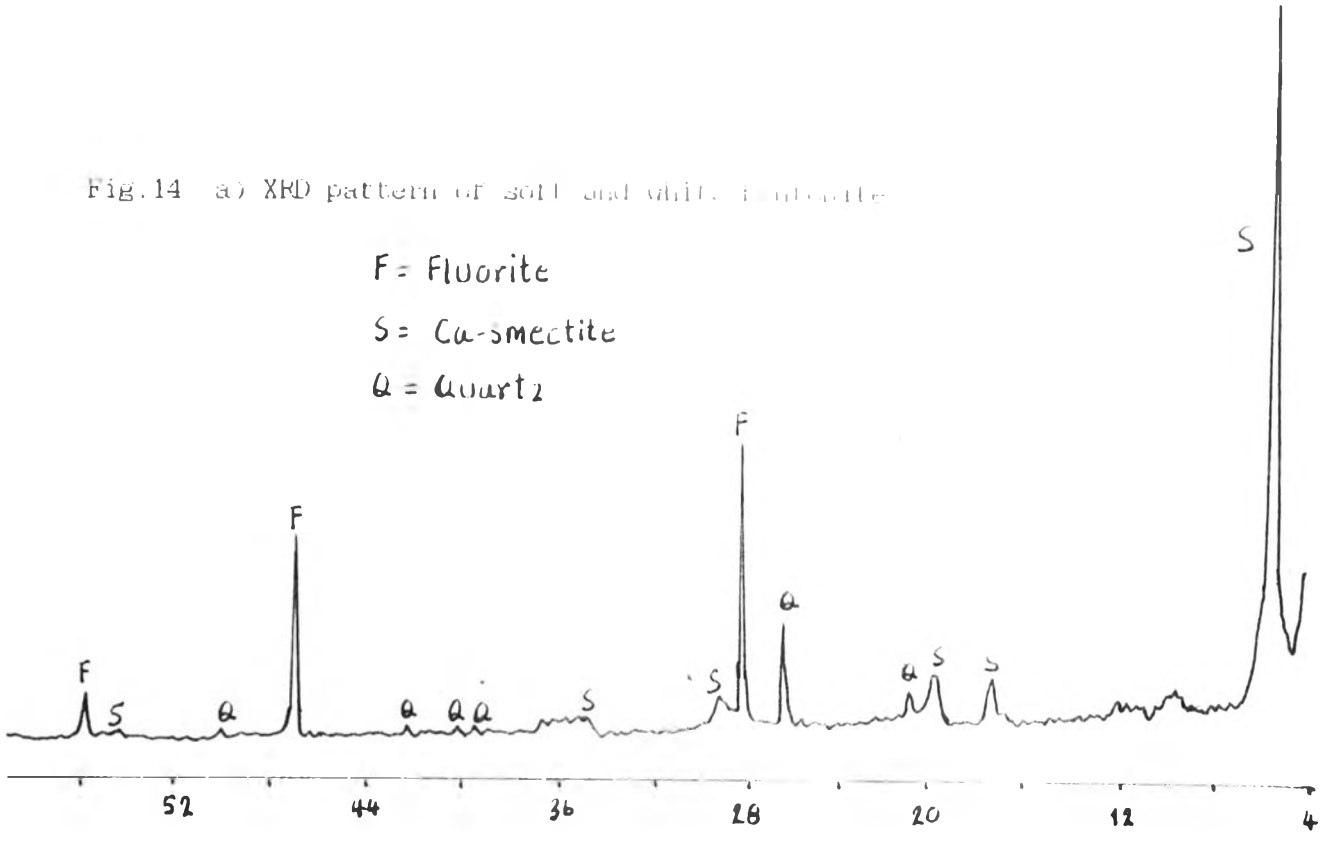

From XRD. pattern of wallastonite, in Fig.15, the major phase was β - $CaSiO_3$ and minor phase was calcite [$CaCO_3$] . The 2θ angles of β - $CaSiO_3$ were :

2θ angle	correspond to	d-spacing
11.50		7.688
16.30		5.433
23.20		3.831
25.30		3.517
26.90		3.312
27.60		3.229
26.90		3.087
30.00		2.974
32.80		2.728
35.00		2.561
35.70		2.513
36.30		2.473
38.40		2.342
39.10		2.302
41.40		2.179
41.60		2.169
42.40		2.130
44.70		2.026
45.70		1.984
49.80		1.829
52.00		1.757
53.50		1.711

The 2θ angles of $CaCO_3$ [calcite] were ;

2θ angle	correspond to	d-spacing
29.50		3.025
32.00		2.794
43.30		2.088
47.40		1.916
48.50		1.875

Fig.15 XRD pattern of wollastonite

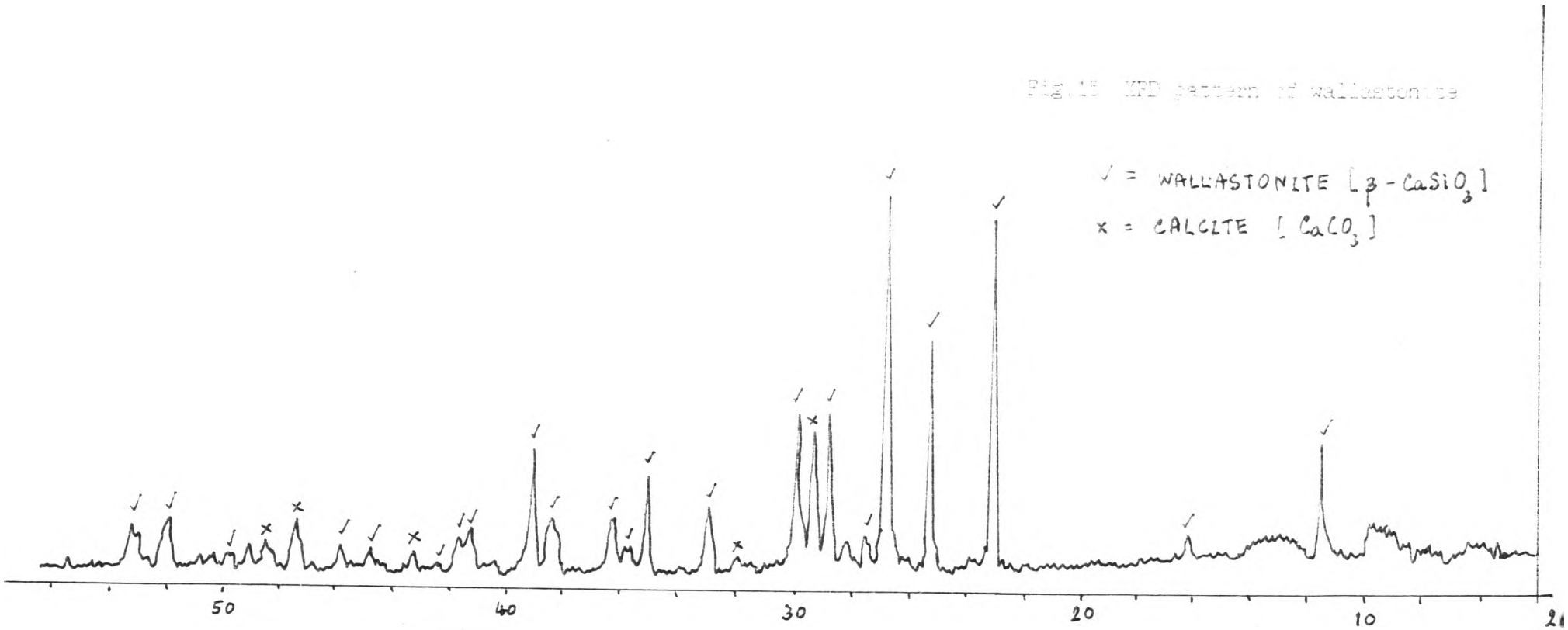

From XRD. pattern of talcum powder, in Fig.16, the major phase was talc [$MgSi_{14}.10\ H_2O$] with minor quartz and magnesite.

The 2θ angles of talc were ;

2θ angle	correspond to	d-spacing
9.50		9.302
19.00		4.667
19.40		4.572
28.60		3.118
34.50		2.597
36.20		2.479
38.50		2.336
40.60		2.220
43.00		2.102
48.60		1.872

THe 2θ angles of quartz were :

2θ angle	correspond to	d-spacing
26.60		3.348
42.50		2.125

The 2θ angles of magnesite [$MgCO_3$] were ;

2θ angle	correspond to	d-spacing
32.60		2.744
43.00		2.102
53.00		1.726

Fig.13 XRD pattern of talcum

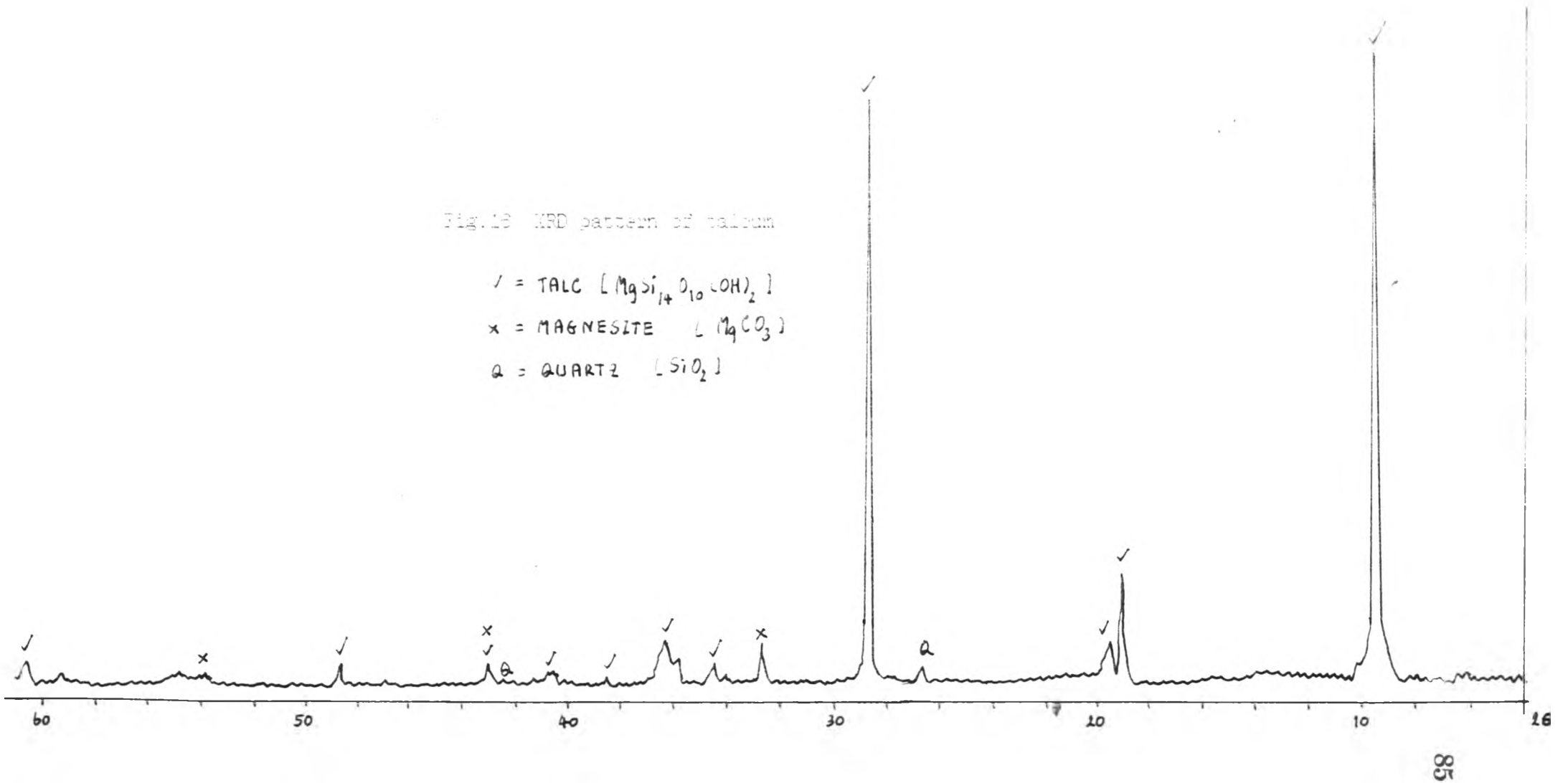

4.2 Grinding and Mixing

4.2.1 Chemical analysis.

Table 11 a) Chemical analysis of compositions.

% Element	LI-22	LI-23
SiO_2	5.960	4.987
Al_2O_3	88.205	90.890
Fe_2O_3	0.086	0.067
TiO_2	0.003	0.003
CaO	0.927	0.546
MgO	1.540	1.590
Na_2O	0.379	0.296
K_2O	0.042	0.028
LOI.	1.831	1.606
Total	99.973	100.000

b) Chemical analysis of LI-23 composition (production) by EDS analysis.

% Element	LI-23 (product)
SiO_2	8.71
Al_2O_3	88.30
Fe_2O_3	0.58
TiO_2	0.25
CaO	0.80
MgO	0.42
Na_2O	0.66
K_2O	0.28
Total	100.00

4.2.2 Density of LI-22 and LI-23 powders.

Table 12 Density of compositions.

no.	LI-22	LI-23
1.	3.59	3.54
2.	3.47	3.65
3.	3.50	3.56
4.	3.44	3.69
average [gm./cm^3]	3.50	3.61

4.2.3 Particle size distribution

Table 13. Particle size distribution of LI-22, LI-23 by pot mill grinding

no.	20 % by weight finer than [micron]
LI-22	1.0 - 1.1
LI-23	1.1 - 1.3

Fig.17 Particle size distribution curve of LI-22 and LI-23 by pot mill grinding

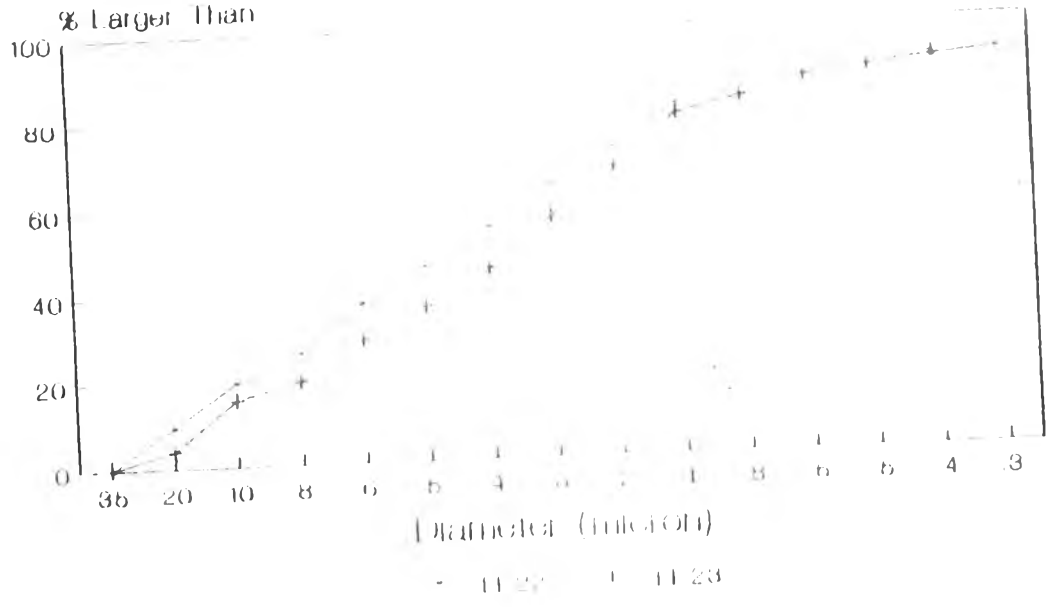

4.2.4 Microstructure of LI-22 and LI-23

From SEM micrographs Fig. 18 , the morphology of powders were irregular shaped of agglomerations.

Fig.18 SEM micrograph of LI-22 and LI-23

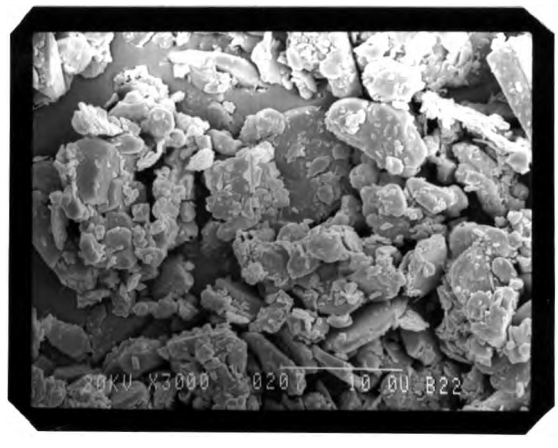

LI-22

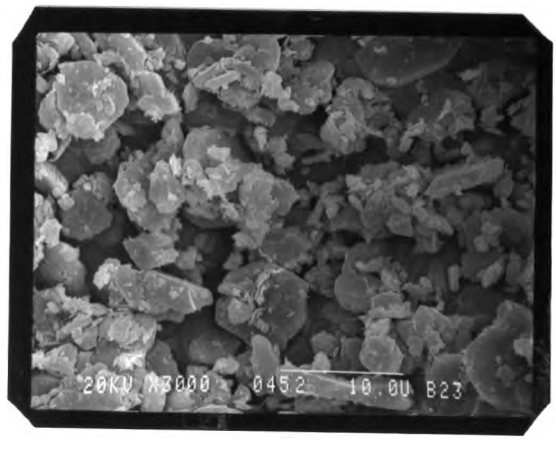

LI-23

4.3 Casting

4.3.1 Specific Gravity of LI-22 and LI-23 slurries.

Table 14.Specfic gravity of composition slurries.

no.	specific gravity
LI-22	1.857
LI-23	1.956

4.3.2 pH of LI-22 and LI-23 slurries

By using pH paper indicator, before adjusting, the slurries had the pH range 8.5 - 9.0, after addition of some hydrochloric acid(dil.) with proper amount that the slurries must not been flocculated. The pH range of the slurries were changed to 7.0-7.5 and could be slip-casted well.

4.4 Properties after Sintering

4.4.1 Weight of specimens

(sintered from the profiled curves A,B,C,D).

Table 15. Weights of specimens.

a). From firing curve A.

LI-22, no.	Dry weight (W)	Saturated weight (M)	Suspended weight (S)
1.	25.62	26.55	18.39
2.	23.94	25.08	17.31
3.	24.85	25.08	17.86
4.	24.88	24.96	17.41
5.	25.29	26.25	18.15
6.	24.22	24.80	17.21
7.	26.62	26.75	18.63
8.	24.97	25.14	17.46
9.	24.74	25.08	17.38
10.	24.93	26.00	17.95
LI-23, 1.	26.22	27.10	18.77
2.	27.72	28.16	19.71
3.	26.23	27.12	18.74
4.	26.67	28.18	19.74
5.	27.70	28.16	19.74
6.	26.13	26.77	18.64
7.	26.22	26.96	18.71
8.	25.29	26.73	18.46
9.	26.47	27.42	18.92
10.	27.68	28.18	19.74

b). From firing curve B.

LI-22, no.	Dry weight (W)	Saturated weight (M)	Suspended weight (S)
1.	37.00	37.01	26.25
2.	37.50	37.94	26.56
3.	35.74	36.29	25.32
4.	39.29	39.47	27.80
5.	29.55	29.86	20.95
6.	37.12	37.72	26.34
7.	40.90	40.94	28.89
8.	34.85	34.97	24.66
9.	34.58	34.60	24.47
10.	38.30	38.94	27.17
LI-23, 1.	35.60	36.99	25.66
2.	39.91	41.45	28.71
3.	39.09	40.64	28.18
4.	39.00	40.02	28.12
5.	40.28	40.71	28.82
6.	38.22	38.41	27.19
7.	40.44	40.97	28.88
8.	39.57	40.30	28.33
9.	38.49	39.62	27.68
10.	37.96	39.33	27.33

c). From firing curve C.

LI-22, no.	Dry weight (W)	Saturated weight (M)	Suspended weight (S)
1.	24.97	24.99	17.85
2.	36.08	36.12	25.73
3.	39.88	39.90	28.34
4.	34.29	34.32	24.36
5.	32.76	32.80	23.26
6.	38.18	38.20	27.30
7.	36.77	36.80	26.27
8.	35.14	35.16	25.14
9.	38.62	38.64	27.64
10.	30.99	31.02	22.16
LI-23, 1.	37.51	37.61	26.74
2.	36.40	36.55	26.05
3.	38.10	38.13	27.39
4.	37.17	37.21	26.65
5.	39.23	39.39	28.06
6.	38.43	38.47	27.64
7.	39.66	39.97	28.38
8.	35.18	35.24	25.15
9.	36.12	36.19	25.72
10.	-	-	-

d). From firing curve D.

	no.	Dry weight (W)	Saturated weight (M)	Suspended weight (S)
LI-22,	1.	29.90	29.91	21.37
	2.	31.85	31.85	22.73
	3.	38.89	38.89	27.77
	4.	34.64	34.64	24.75
	5.	39.32	39.32	28.10
	6.	37.47	37.47	26.76
	7.	32.49	32.50	23.21
	8.	34.44	34.44	24.62
	9.	37.10	37.10	26.40
	10.	32.82	32.82	23.44
LI-23,	1.	37.85	37.86	27.15
	2.	41.40	41.41	29.69
	3.	37.74	37.75	27.10
	4.	40.58	40.58	29.03
	5.	37.14	37.14	26.64
	6.	41.21	41.21	29.60
	7.	42.82	42.82	30.70
	8.	33.37	33.37	23.94
	9.	42.43	42.44	30.53
	10.	36.85	36.86	26.48

4.4.2 % Shrinkage of specimens sintered from curve D were presented in Fig.19, from the graphs , the average shrinkage of LI-22 and LI-23 specimens at this firing condition were in the range 21.540 ± 0.075 and 21.320 ± 0.941.( ] = standard deviation from 10 specimens.)

The LI-23 specimens had less % shrinkage than the LI-22 specimens because of lower % ball clay and bentonite.

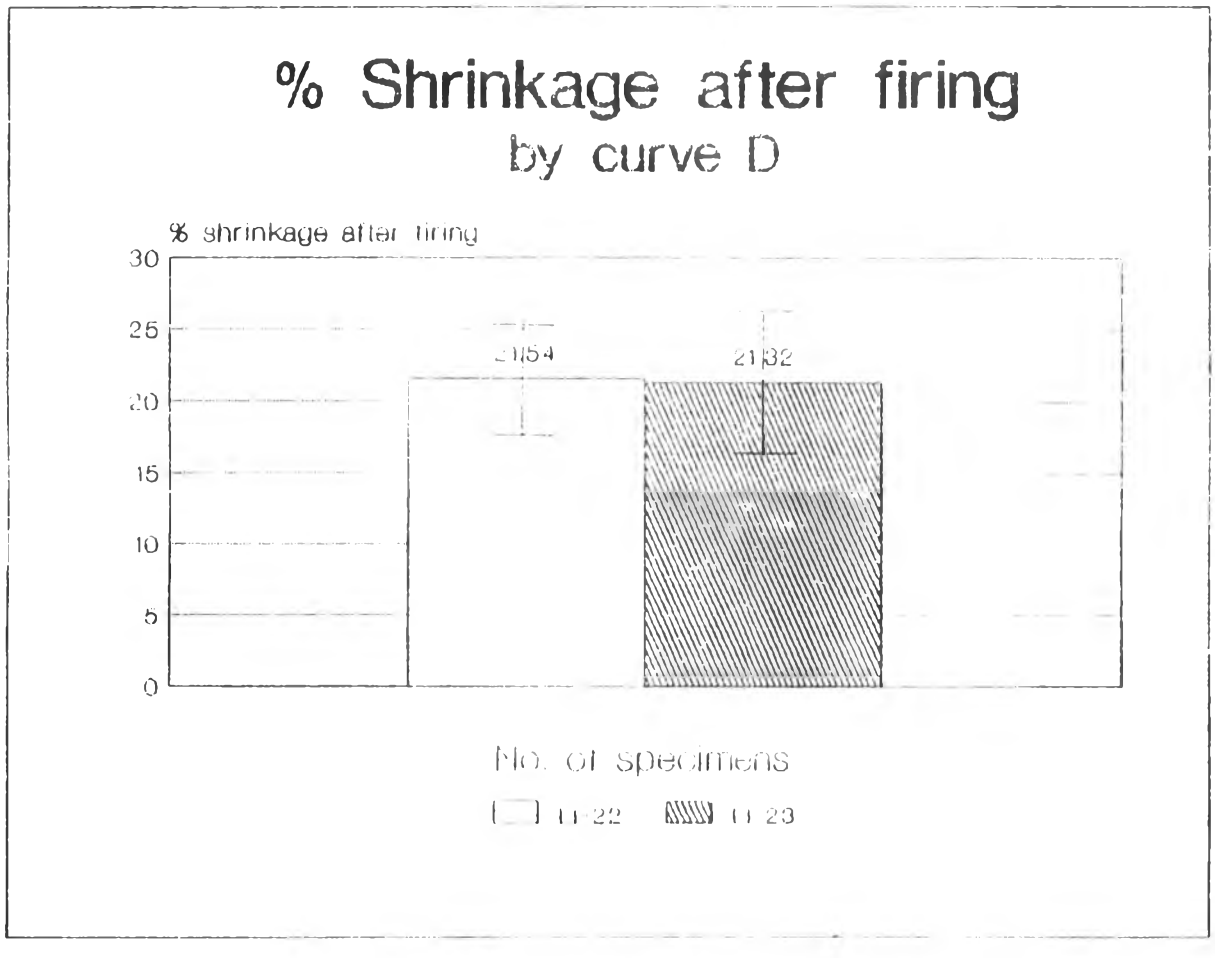

Fig.19 %Firing shrinkage of specimen

4.4.3 Calculations of volume (V), bulk density (D), % apparent porosity (P) and % water absorption (A).

[The datas were shown in appendix 3]

The relation between firing conditions and bulk density, % apparent porosity, and % water absorption were presented in the graphs in Fig. 20. From these graphs, as the sintering temperature increased, the density also increased whilst the % apparent porosity and % water absorption decreased. (I = standard deviation from 10 specimens).

The LI-22 and LI-23 specimens sintered at 1520° C. with 3 hours soaking period [firing curve D.] gave the best results that the % water absorptions were zero, and the average densities of both compositions were(3.497 ± 0.011) gm./cm.^{3} and (3.540 ± 0.013)gm./cm.^{3} respectively.

The LI-22 and LI-23 specimens sintered from curves A, B, and C still had high percentage of both porosity and water absorption.

Fig.20a Relation between firing condition and bulk density

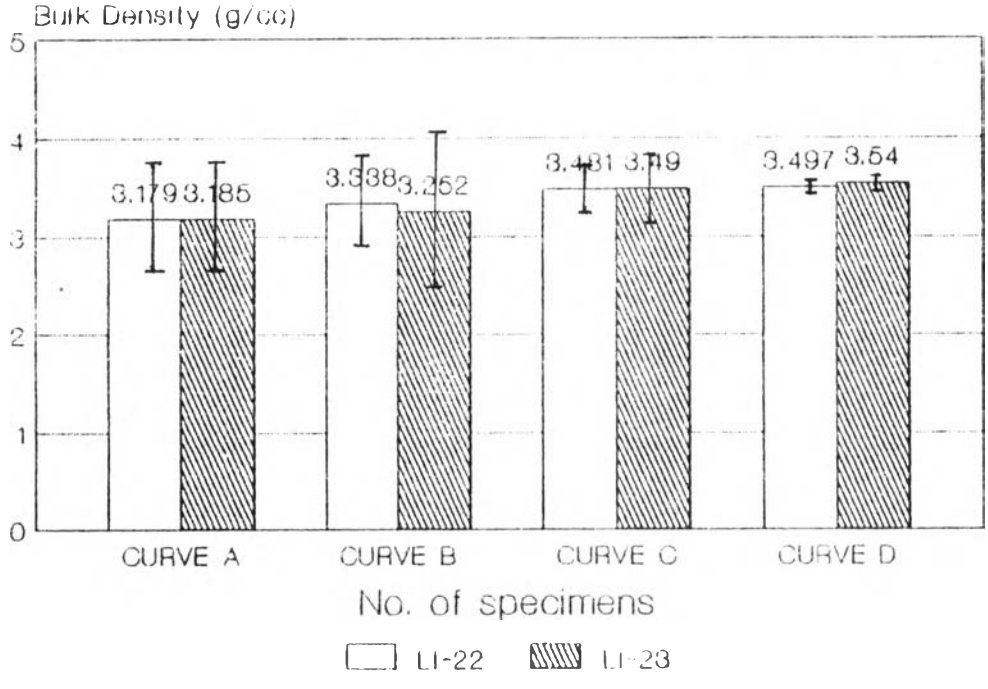

Fig. 20b Relation between sintering condition and % apparent Porosity.

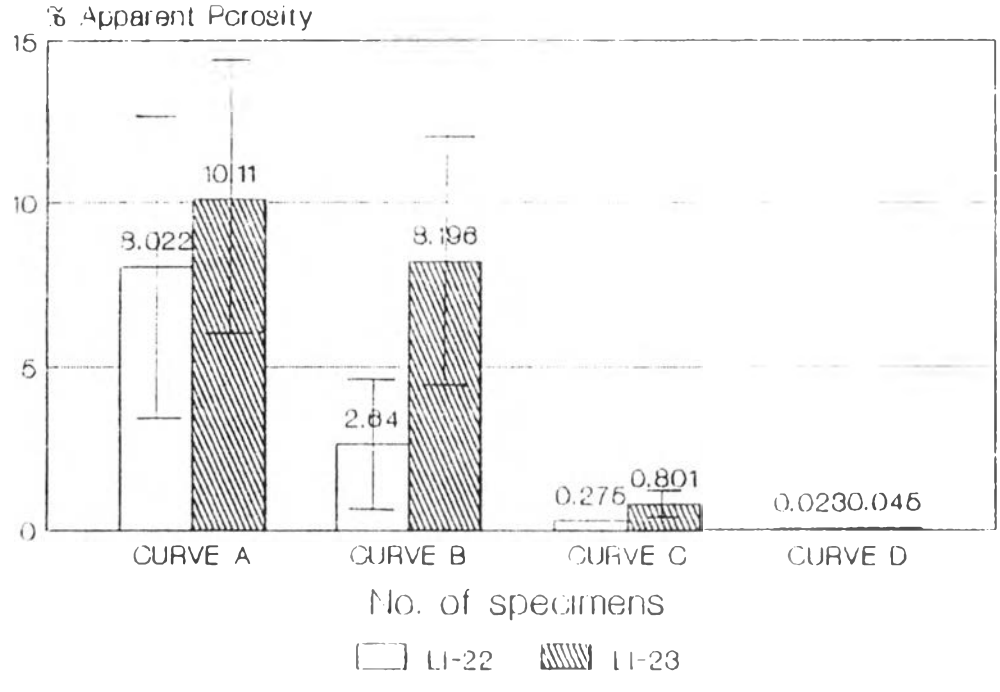

Fig. 20c Relation between sintering condition and % water absorption.

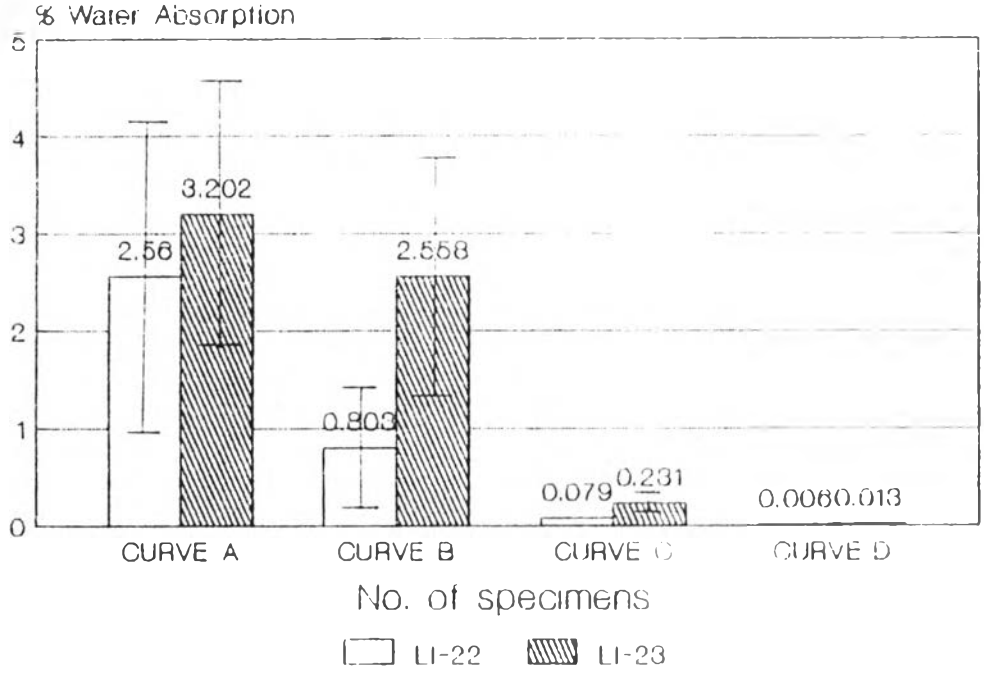

% Water absorption of the liners, firing from curve D

Table 16. % Water absorption of products.

no.	W(gm.)	M(gm.)	% Water absorption
1.	781.0	781.0	0.000
2.	781.5	782.2	0.089
3.	777.2	777.6	0.051
4.	773.0	773.7	0.091
5.	759.0	759.3	0.039
6.	745.0	745.0	0.000
7.	787.0	787.0	0.000
8.	784.2	784.2	0.038
9.	782.5	782.7	0.026
10.	782.0	782.2	0.026
average			0.036 %

The results were agreed with the specimens testing.

4.4.4 Modulus of rupture

The relation between MOR and firing conditions of LI-22 and LI-23 were presented in Fig.21(⌶ = standard deviation) The influence of sintering temperature and time to the strength (MOR) of specimens were,

1) when temperature increased from 1500°C.[curve A] to 1520°C.[curve C], the average MOR. of LI-22 increased from 2656.07 kg./cm.^{2} to 2868.99 kg./cm.^{2}, and for LI-23 the average MOR increased from 2593.88 kg./cm.^{2} to 2704.38 kg./cm.^{2}

2) If soaking time at the maximum temperature increased, the MOR also increased as shown from the MOR result between firing from curve A and B, or curve C and D of both compositions.

3) The average MOR of LI-22 and LI-23 were both over 3000 kg./cm.^{2} which could be accepted comparing to the MOR of the commercial liners, these resulted by firing to 1520°C. with 3 hours soaking period and also agreed with 0% water absorption.

The MOR datas were presented in appendix 4.

Fig. 21 The relation between firing condition and MOR

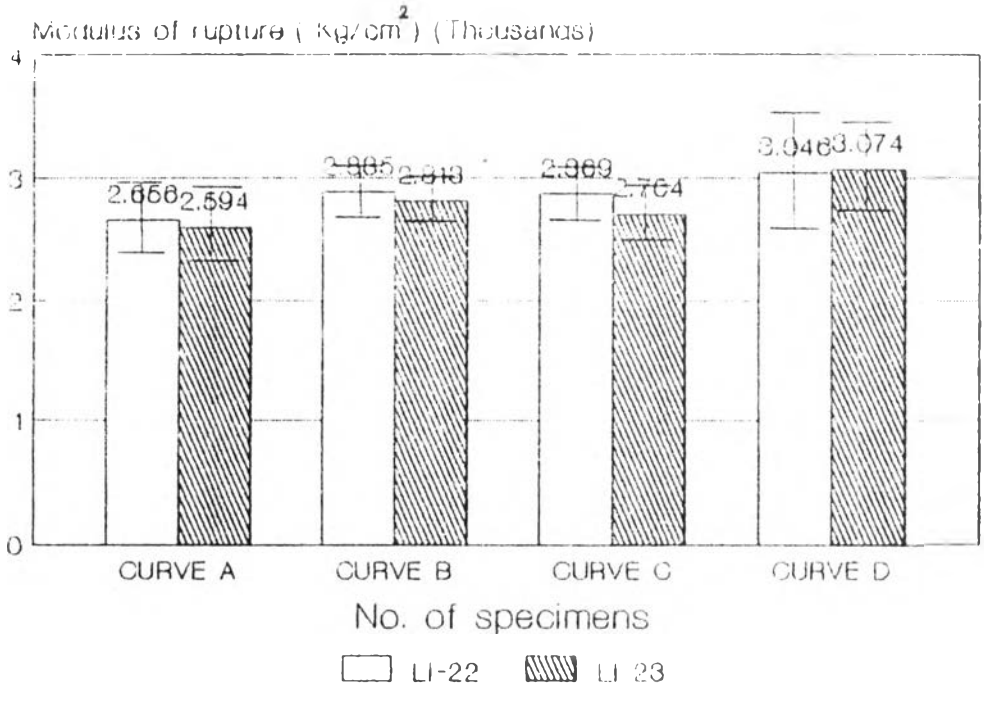

4.4.5 Coefficient of linear thermal expansion of the LI-22 and LI-23 specimens, sintered at 1520°C. with 3 hours soaking period [curve D], were calculated from the % linear thermal expansion .

A dilatometer was used to mearure the % expansion of the LI-22 and LI-23 specimens (sintered from curve D.) by heating to 1000° C. at 3°C./minute. The plots connecting percent expansion and temperature (°C.) were illustrated in Fig. 22.

Both specimens gave a straight-line thermal expansion curve (on heating).The values of thermal expansion were calculated in the temperature range of 250° C. to 800°C. with correction factor of this dilatometer (A = 0.032) ;

The COE. of LI-22 = 9.02 x 10^{-6} in./in.° C.

and LI-23 = 8.91 x 10^{-6} in./in.° C.

The COE. of both composition were nearly the same.

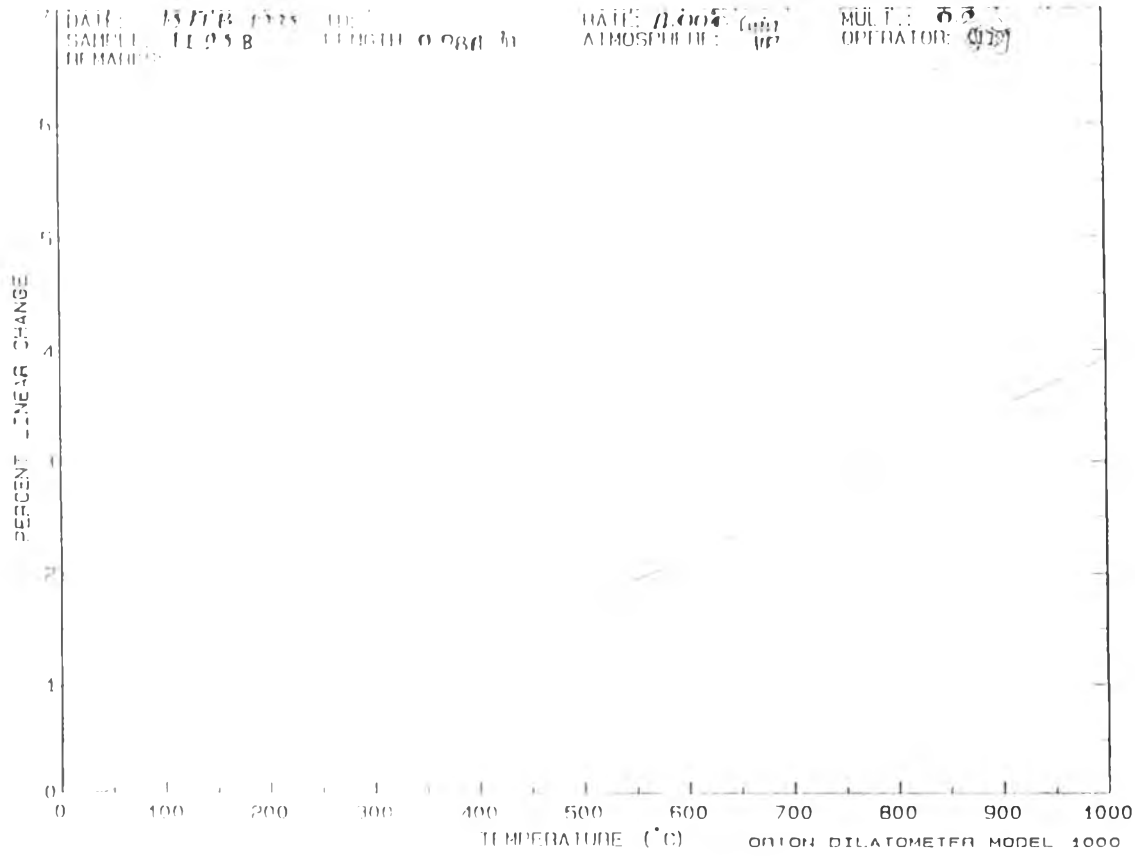

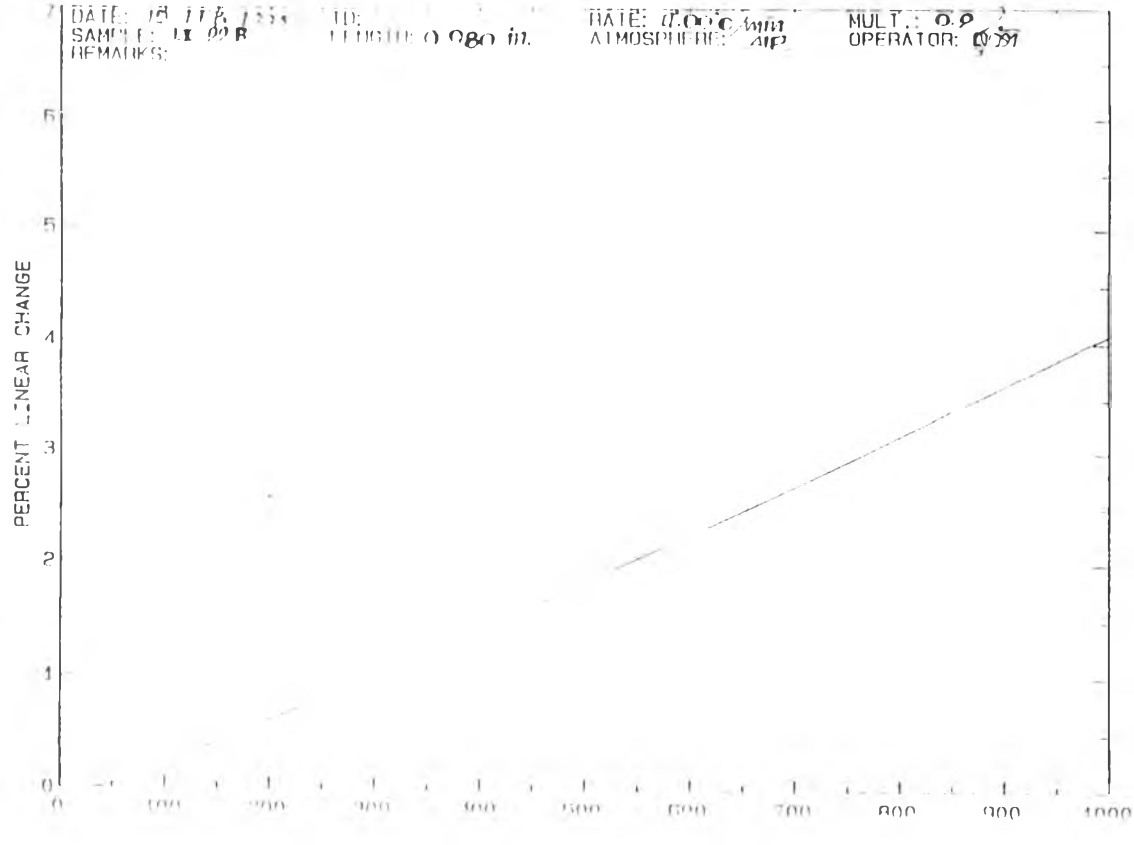

Fig.22 Relation between % linear thermal expansion and temperature

4.4.6 Microstructure of LI-22 and LI-23 specimens.

Some pieces of specimens after firing from various temperatures were broken and the fracture surfaces were examined for the grain structure and pores by SEM in Fig. 23.

The SEM micrograph shown that with increasing temperature, or soaking period, the % pore volume was decreased and the grain structure of alumina became to be massive formed.

Fig. 23 SEM micrographs of specimens. a) LI-22

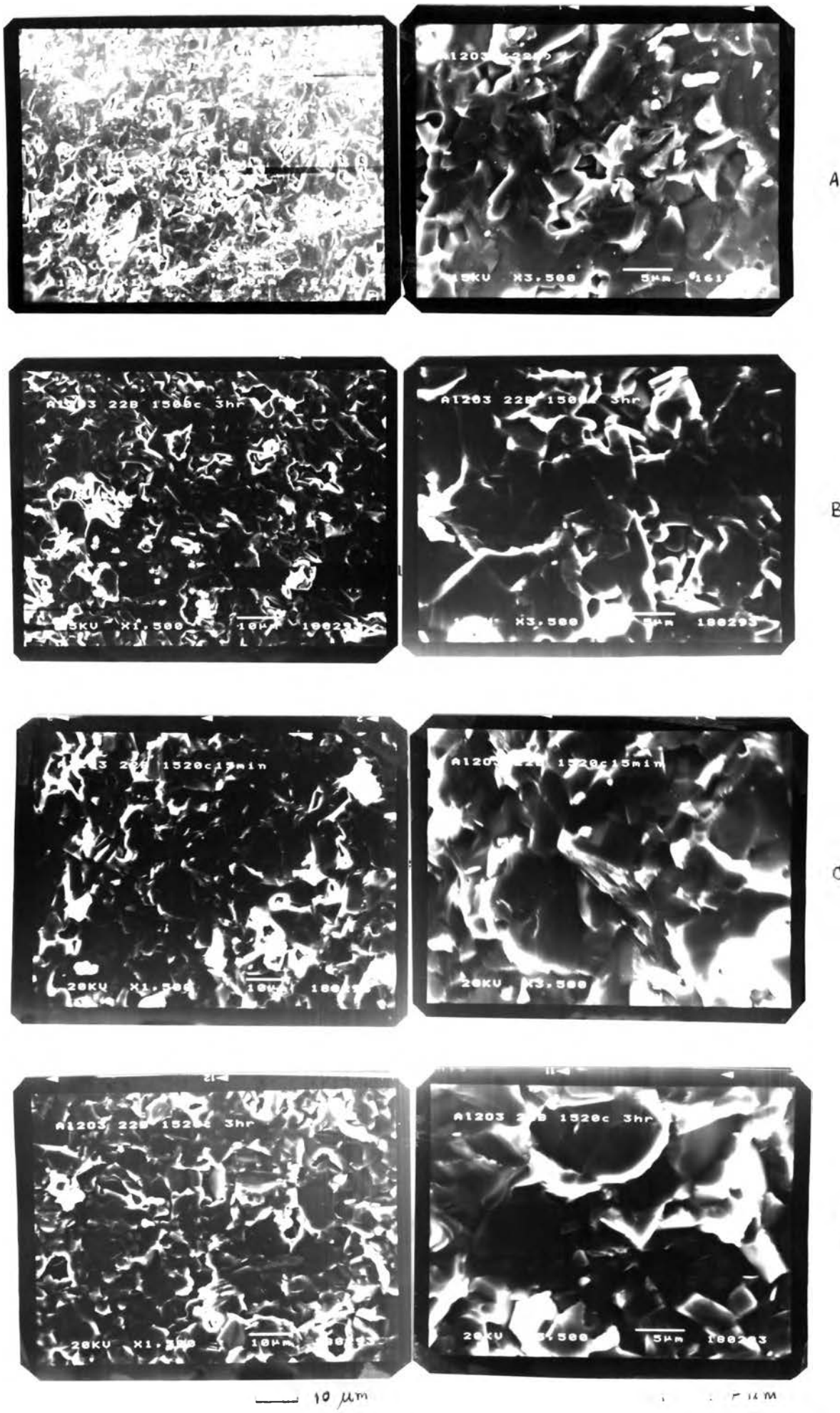

b) LI-23

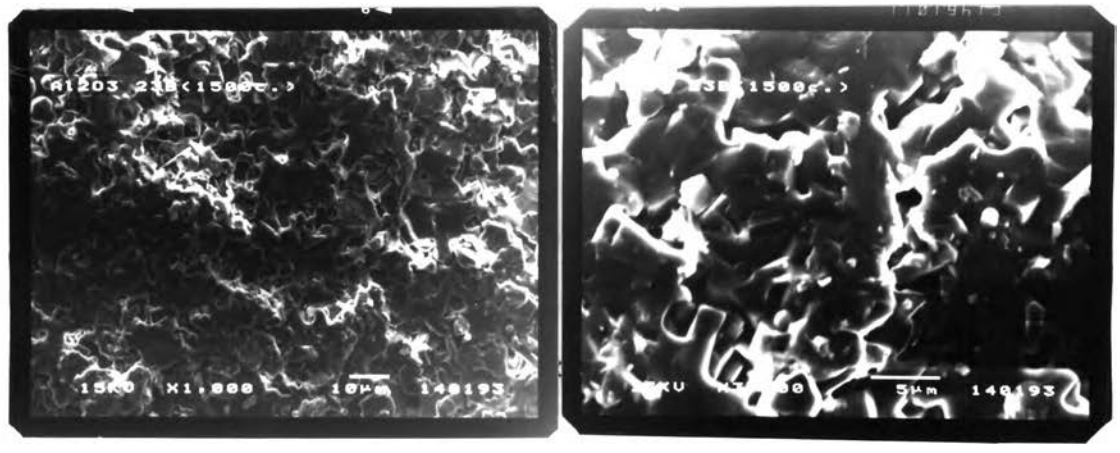

A

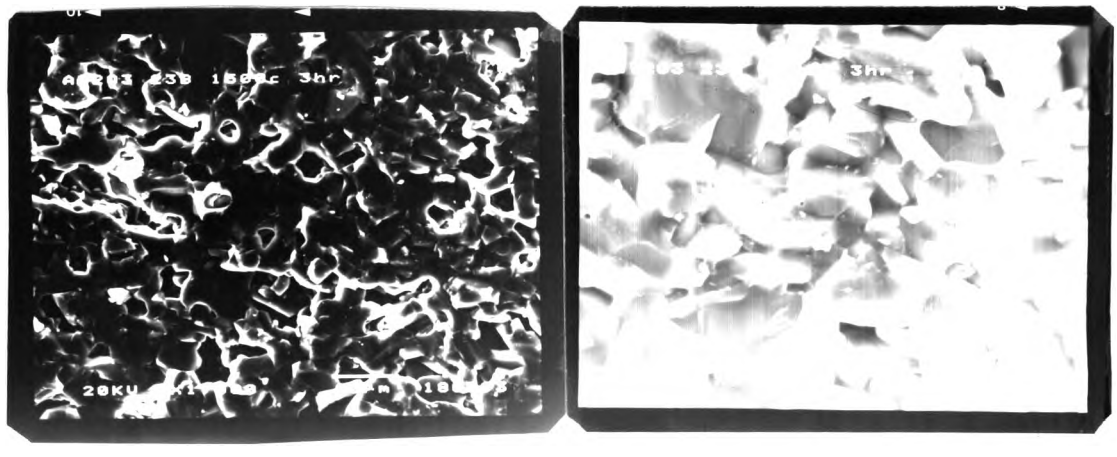

B

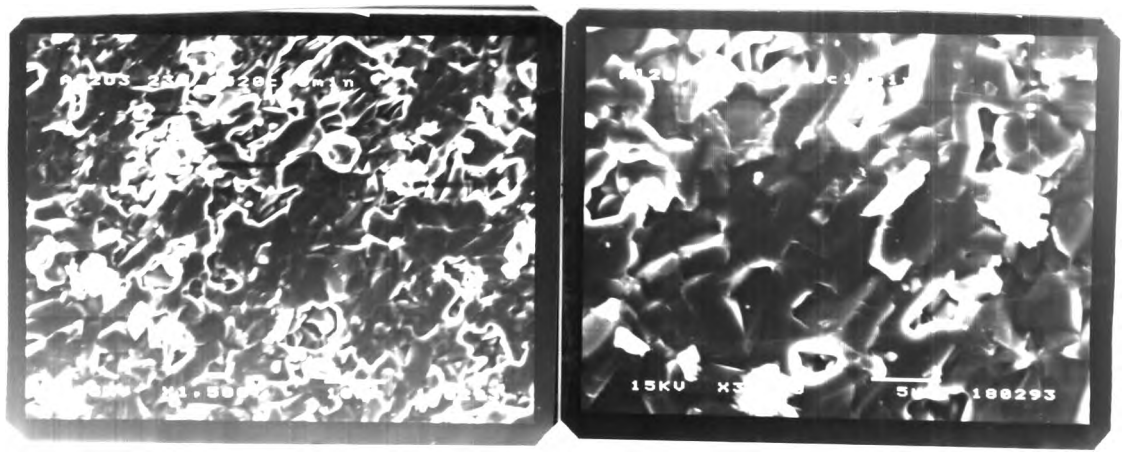

C

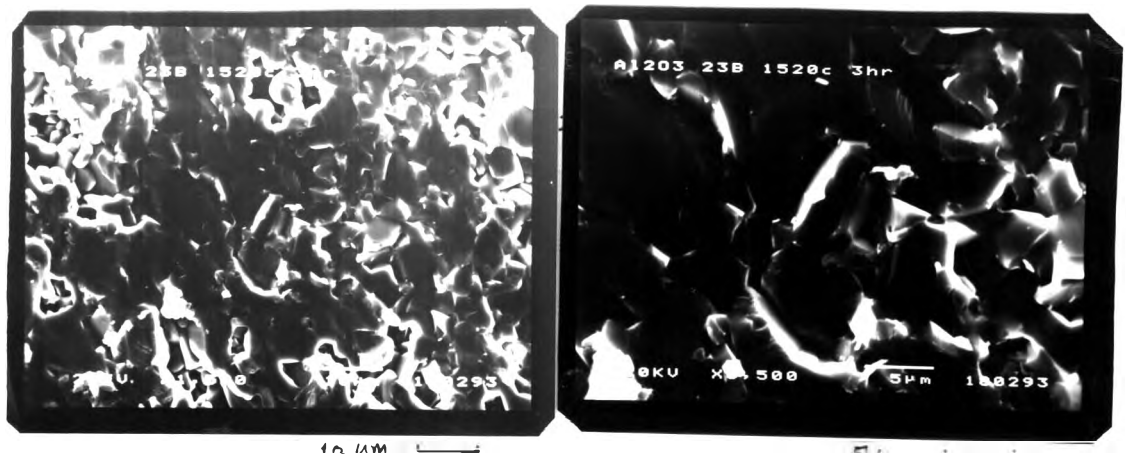

D

10 µm

Microstructure of the liner-product.

The difference in microstructure between rim and center might be caused by sintering behavior. The sintering temperature at rim might be higher than at center, this agreed with the EDS analysis that the %alumina at rim was lower comparing to the center.

Fig.24 SEM micrograph of liner product

rim

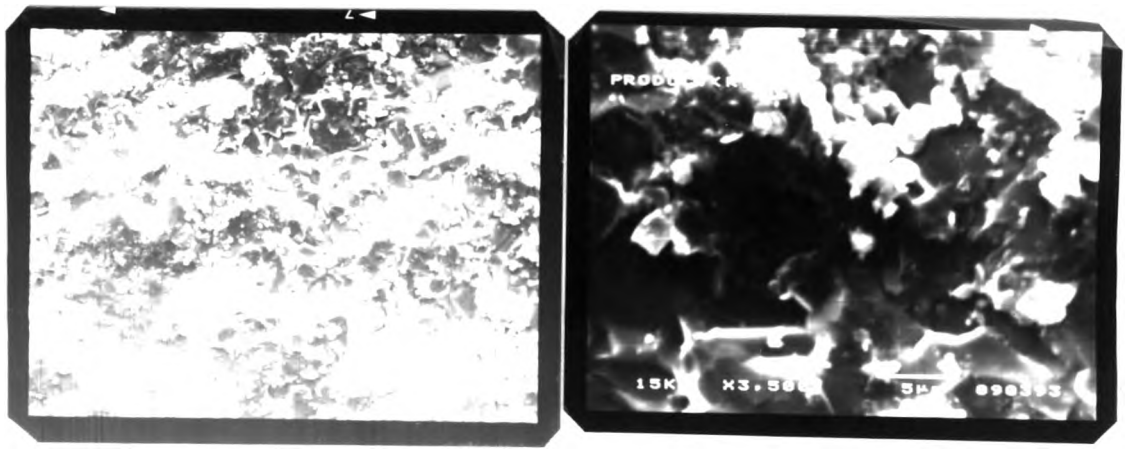

center

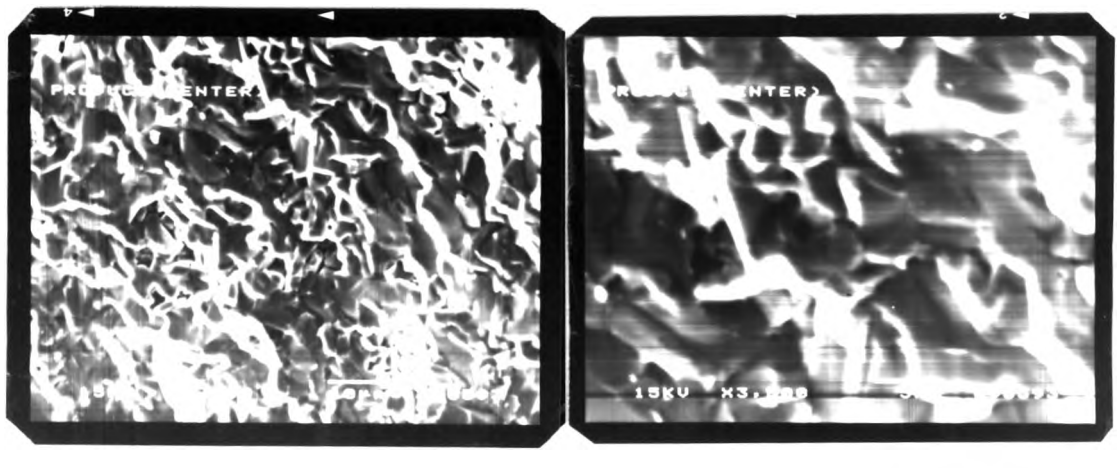

10 μm 5 μm

The approximation of % pore volume = 13.3 % , as presented in Fig.25, and the edge and rim of grain structure shown in Fig. 26, were round, partially dissolved.These resulted from good sintering condition.

Fig.25 Microstructure examination of liner (x100), showed pore structure.

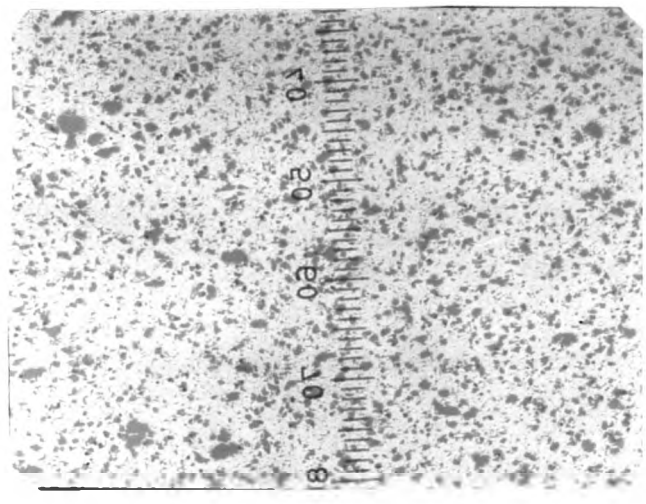

Fig.26 Microstructure examination of liner (x100), showed grain structure.

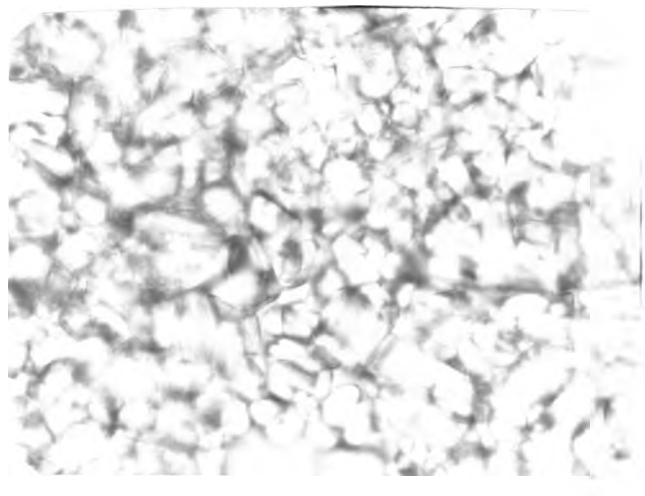

4.4.7 EDS analysis

Table 17. EDS. analysis of specimens.

a). From firing curve A.

% Element	LI-22	LI-23
Al_2O_3	85.190	88.490
SiO_2	10.880	9.778
CaO	1.460	1.303
MgO	0.690	-
Na_2O	0.700	-
K_2O	0.210	-
Fe_2O_3	0.560	-
TiO_2	0.310	0.430
Total	100.000	100.000

b). From firing curve B.

% Element	LI-22	LI-23
Al_2O_3	85.760	89.32
SiO_2	10.100	8.240
CaO	1.280	0.860
MgO	1.170	-
Na_2O	0.600	0.570
K_2O	0.160	-
Fe_2O_3	0.660	0.630
TiO_2	0.270	0.380
Total	100.000	100.000

c). From firing curve C.

% Element	LI-22	LI-23
Al_2O_3	86.900	88.600
SiO_2	10.080	9.030
CaO	1.520	0.870
MgO	0.320	0.240
Na_2O	0.460	0.610
K_2O	0.100	-
Fe_2O_3	0.380	0.650
TiO_2	0.240	-
Total	100.000	100.000

d). From firing curve D

% Element	LI-22	LI-23
Al_2O_3	82.940	87.820
SiO_2	14.200	10.110
CaO	1.520	0.740
MgO	0.410	0.210
Na_2O	0.170	0.220
K_2O	-	0.210
Fe_2O_3	0.760	0.440
TiO_2	-	0.250
Total	100.000	100.000

EDS analysis of the liner-product, firing from curve D.

Table 18 EDS. analysis of product.

Element	Rim	Center
Al_2O_3	87.61	90.59
Sio_2	10.36	7.01
CaO	0.70	0.58
MgO	-	-
Na_2O	0.60	1.00
K_2O	0.09	-
Fe_2O_3	0.64	0.54
TiO_2	-	0.28
Total	100.00	100.00 %

EDS pictures of LI-22 and LI-23 and liner-product were presented in appendix 7

4.4.8 From XRD. patterns of the LI-22 ,LI-23 specimens sintered from firing curves A, B, C, and D, and liner-product, sintered from firing curve D, the phases presented that the major phase were still dominantly α -Al_2O_3 with some minor phases of spinel, $MgAl_2O_4$.

These meant that MgO from talcum, added to alumina, caused spinel formation (around 700 C.) which was not soluble in alumina at temperature below 1700 C.

By comparison to the XRD patterns of starting α -Al_2O_3, and the liner-product, the height of α -Al_2O_3 peaks in the liner-product were a little bit higher. This meant that after sintering, the size of alumina grains were bigger.

The XRD patterns of LI-22 and LI-23 and the liner product were presented in Fig. 27a) ,27b) and 27c)

The XRD patterns and the values of 2θ angles with d-spacing values of α -Al_2O_3 phase and spinel phase in the liner-product were presented in appendix 8.

Fig. 27C) XRD pattern of product

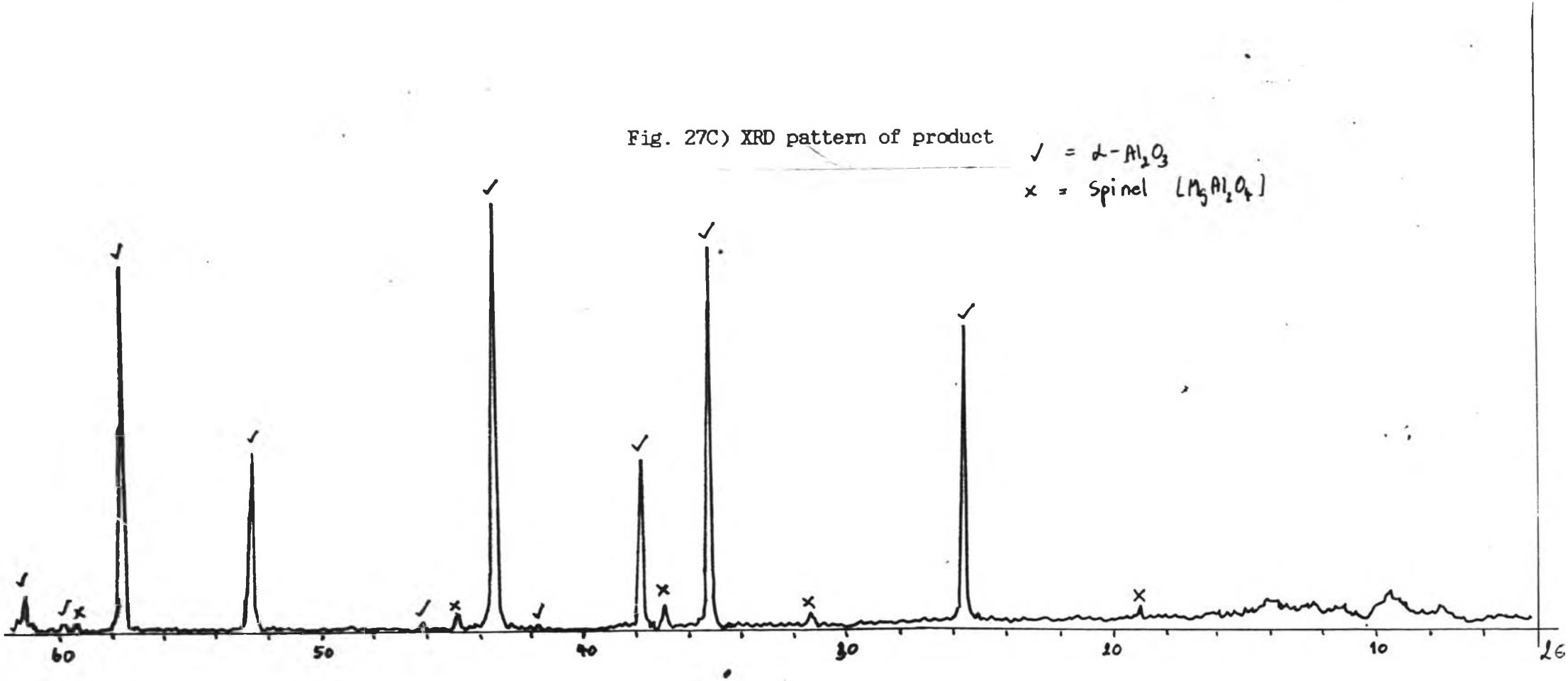

Fig. 27a XRD pattern of LI-22 specimens

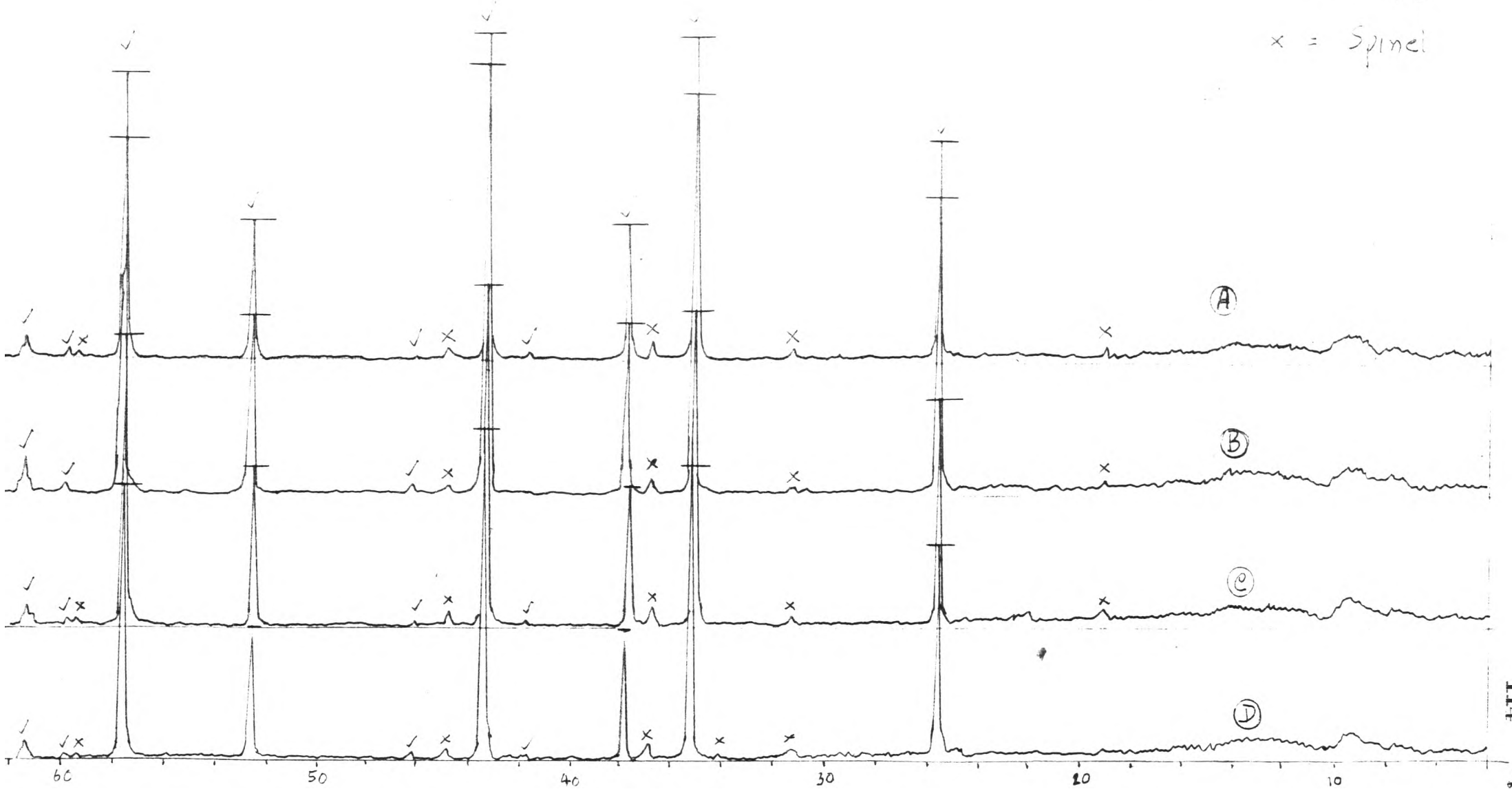

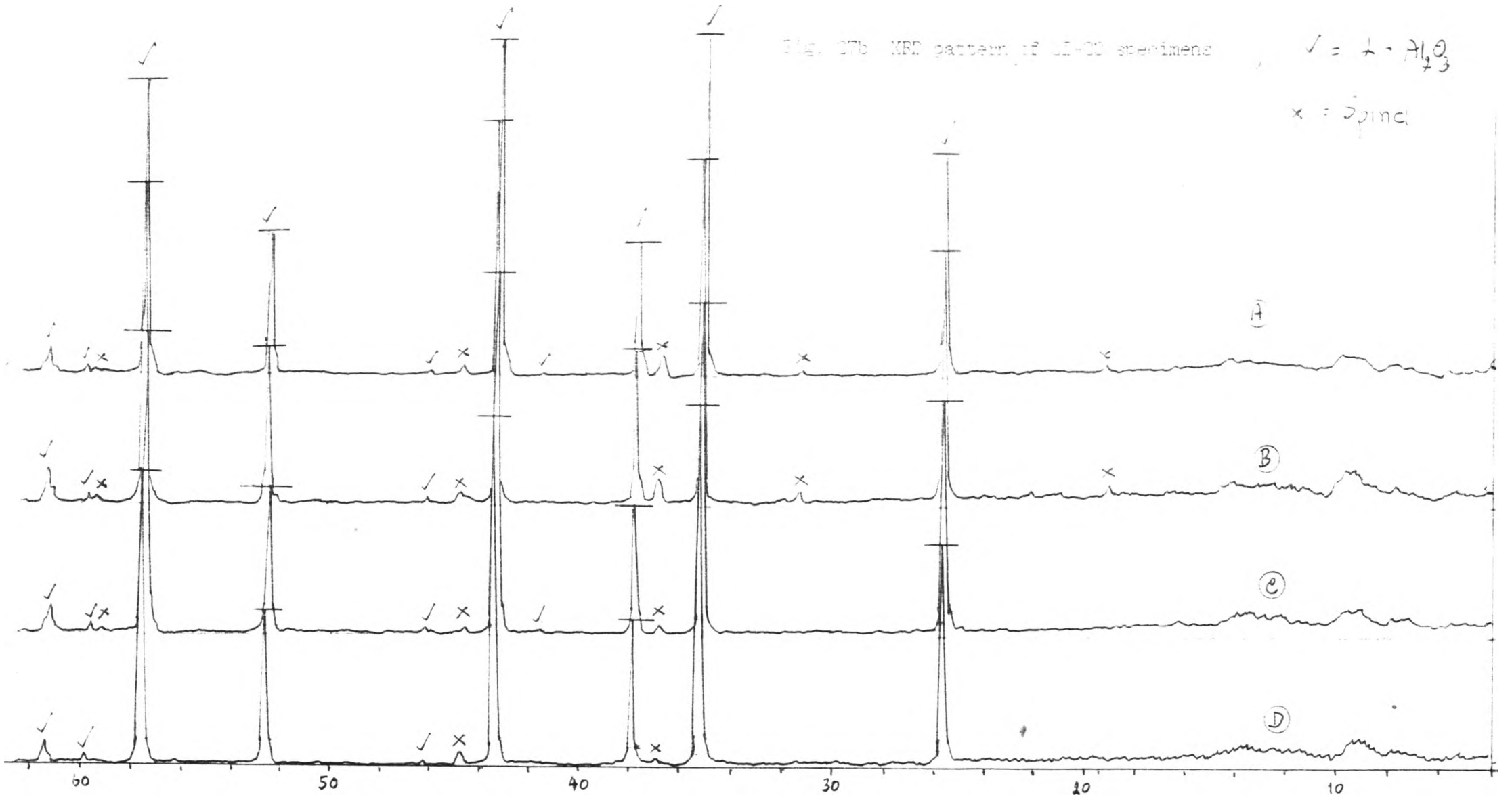
Fig. 37b XRD pattern of CA-20 specimens
✓ = α - Al2O3
× : Spinel
A
B
C
D
60
50
40
30
20
10

4.4.9 Hardness.

Rockwell hardness test ; an indentation hardness using a verified machine to force a diamond indenter under specified conditions, into the surface of the sample under test in two operations, and to measure the different in depth of the indentation under the specified condition preliminary and total test forces [minor and major load respectively].

[Test method according to ASTM. Designation: E 18-89a.]

The Hardness [HR45N] results were ;

no.1	=	76.8
no.2	=	76.6
average	=	76.7

Indenter	;	Diamond cone
Load	;	45 Kg.
Duration time	;	-

The average hardness value of the liner-product was 76.7,compared to the commercial liners,this value was accepted.

4.4.10 Wear Resistant ; Abrasion test.

The starting weights and weight loss [in gm.] of rapid pot mills [400 rpm.] from different firing curves were presented as followed ;

Table 19. Data of weight loss in 48 minutes/cycle from abrasion test.

Firing curves.	A.	B.	C.	D.
Starting weight[gm.]	2080	2068	2075	2040
After grinding, 1st.	2066	2057	2067	2032
2nd.	2054	2045	2060	2025
3rd.	2045	2036	2055	2019
4th.	2037	2027	2048	2014
5th.	2025	2020	2042	2009
6th.	2010	2013	2037	2004
7th.	2000	2007	2030	2000
8th.	1997	2002	2024	1997
9th.	1990	1998	2020	1994
10th.	1980	1995	2017	1991
11th.	1975	1992	2014	1988
12th.	1969	1989	2011	1985
Total weight loss. in 12 cycles [gm.]	111	79	64	55

The % wt.loss /hour in 400 rpm. testing were calculated and presented in appendix 5.

The relation between % wt.loss/hr. and firing temperature were presented in Fig. 28 and Table 20.

Table 20. Relation between % wt.loss / hr. and firing condition.

Firing condition	% wt,loss/hr. by 400rpm.
A	0.5559
B	0.3979
C	0.3213
D	0.2808

According to the values of density, % apparent porosity, and % water absorption, these could be concluded that the sintering temperature at 1520° C. with 3 hours soaking period resulted in the lowest of % wt.loss/hr. of the body.

Fig.28 Relation between firing condition and % wt. loss/hour (400rpm)

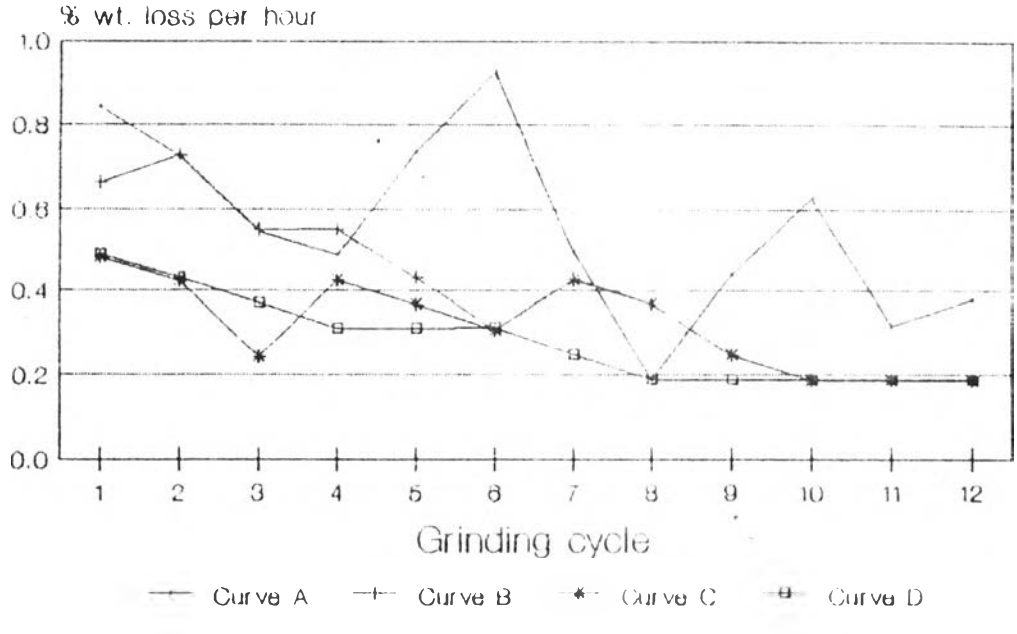

4.5.11 Impact Strength.

According to ASTM Designation : E 23, the impact energy of LI-23 specimens were presented in graph in Fig. 29. (the data was shown in appendix. 6)

From this figure, the values of impact energy of the liner-product sintered from firing curve D.were in the range of (9.80 ± 1.50) kp.cm./cm.^{2} (∫ = standard deviation).This relation could not be clearly concluded because there were some variations in size and surface of the specimens eventhough those specimens were all well prepared by grinding.

With comparison to the commercial liners which had impact energy = 8 kp.cm/cm^2 ,the impact energy of the liner-product from this experiment was accepted.

Fig.29 Impact energy of liners.

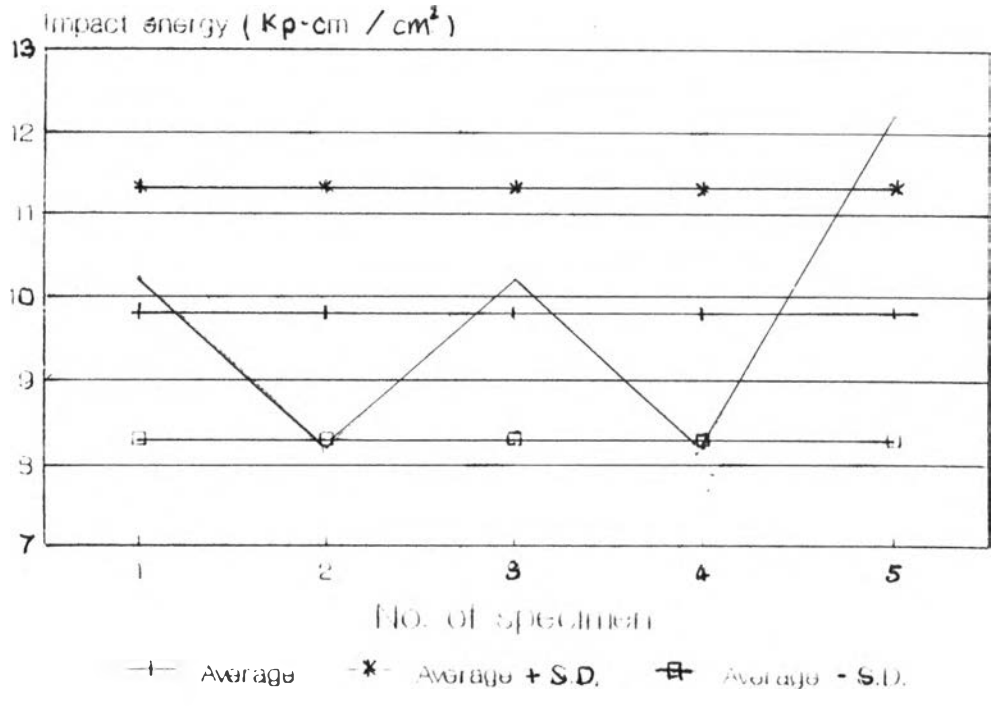

Typical Physical Properties of Liner from Experiment

Forming method	extrusion
% Al_2O_3 content	88-90
Density [gm./cm.^{3}]	3.540
Hardness [Rockwell 45N]	76.7
MOR. [gm./cm.^{3}]	3074
% water absorption	0
Impact strength [kp.cm/cm^2]	9.80
% weight loss/hour [400rpm]	0.2808
colour	white